Energy Advances

ROYAL SOCIETY OF CHEMISTRY

PERSPECTIVE

View Article Online
View Journal | View Issue

Cite this: *Energy Adv.*, 2024, 3, 1238

The energy storage application of core-/yolk–shell structures in sodium batteries

Anurupa Maiti, * Rasmita Biswal, Soumalya Debnath and Anup Bhunia *

Materials with a core–shell and yolk–shell structure have attracted considerable attention owing to their attractive properties for application in Na batteries and other electrochemical energy storage systems. Specifically, their large surface area, optimum void space, porosity, cavities, and diffusion length facilitate faster ion diffusion, thus promoting energy storage applications. This review presents the systematic design of core–shell and yolk–shell materials and their Na storage capacity. The design of different metal structures with different shapes and their corresponding synthesis methods are also highlighted. Moreover, changes in capacity with a variation in the carbon moiety and porosity in terms of applications are highlighted. Furthermore, to compete with the dominant Li batteries in the market, materials with low-cost large-scale production and high active mass loading need to be developed. Thus, both yolk- and core–shell structures have been designed considering their significant structural advantages for application in Na batteries and their impacts on the rate capacity and reversible capacity. This review also demonstrates the advantages of yolk–shell and core–shell structures in faster Na ion transportation and excellent cycling stability. Furthermore, the synergistic effect of the core–shell structure enhances reversible capacity. Additionally, the conducting coating of the encapsulated structure increases electron transport, and a higher exposure of the electrode to the electrolyte is further beneficial for the growth of a stable SEI layer. Considering these advantages and disadvantages, this review may help guide the future advancement of sodium batteries (SIBs) in upcoming research based on the advantages of the core–shell and yolk–shell morphology. Finally, future perspectives regarding machine learning (ML) to access better performances in Na batteries are discussed.

Received 29th February 2024,
Accepted 12th May 2024

DOI: 10.1039/d4ya00141a

rsc.li/energy-advances

1. Introduction

The storage of sustainable energy has become an important topic owing to the increasing demand for renewable clean energy in daily life. In this case, high-temperature (HT) Na–S battery technology was first developed for application in electric vehicles (EV) by Ford Motor Company in 1966.[1] Faradion (UK), Novasis (USA), HiNa (China), and Tiamat (France) are some of the renowned companies who have evolved their expertise towards sodium battery technology in the last few years.[2] The leading Chinese company CATL (market value of almost $200 billion) is focused on developing batteries with high energy density, reaching 160 W h kg^{-1} to date, and is targeted to reach a value of 300 W h kg^{-1} for sodium batteries.[3] Moreover, the Chinese automaker JAC Group and tech company 'HiNa Battery' developed Na-battery technology named 'Hua Xianzi', a compact electric vehicle that can travel 155 miles on a single charge.[3] Most sodium battery startup companies were established after 2010, and by 2030, the Na e-vehicle will be a new market competitor to Li-ion batteries. The Na-ion battery company manufacturers have started their business with the total market value of 6–60 billion RMB (Renminbi, official currency of China), except for CATL (1329.643 billion RMB).[3]

Recently, numerous advancements have been made in battery technology and its different integral systems. Multifold modifications are employed on different battery components such as the anode, cathode, electrolyte, membrane, and thermal management system. Researchers have employed different technologies in several battery systems to enhance their performance. In the last decade, numerous reviews and publications have focused on the components of sodium batteries such as their separator, cathode, anode and electrolyte.[1,4] Alternatively, herein, we highlight the various aspects of the sodium battery briefly. Importantly, the focus of this review is to help guide the selection of appropriate cathodic and anodic materials based on a thorough survey of the previous literature.

Sodium (Na) is a much cheaper metal compared to lithium (Li), potassium (K), and magnesium (Mg) and its redox potential is comparatively more positive [$E^{\circ}(Na^{+}/Na^{0})$ = −2.71 V *vs.* the standard hydrogen electrode] than that of Li metal.[1]

Department of Chemical Sciences, Indian Institute of Science Education and Research, Kolkata, India. E-mail: anu.inorganic@gmail.com, bhunia1988@gmail.com, rs.biswal14@gmail.com, soumalyabethua@gmail.com

Hence its operating voltage window (greater than 2 V can be considered), theoretical capacity (1672 mA h g^{-1}) and operating temperature (operating at 20–300 °C) will facilitate a higher capacity compared to lithium.[1] However, the ionic radius of sodium is larger (1.02 Å) than that of lithium (0.76 Å) and it is heavier (Na: 23 g mol^{-1} *vs.* Li: 7 g mol^{-1}), consequently producing a lower volumetric capacity.[5] However, despite these shortcomings, it is interesting to note that metallic Na is abundant and cheap compared to Li and due to its low cost and toxicity, it is an ideal alternative for the future production of electrical vehicles (EV).[6] Moreover, lithium extraction from mines is very costly, laborious and produces huge CO_2 emissions.[7] Hence, lithium batteries are not ecofriendly and their main cathodic components such as cobalt and nickel are also carcinogenic elements. Importantly, the melting point of sodium is higher than that of lithium, and thus it can operate at very high temperatures (above 300 °C). Sodium batteries are also less explosive in a higher temperature range and can operate in a wide temperature range of 20 °C to 300 °C. Therefore, for long-distance travel, the decrease in capacity is less associated with temperature. Hence, sodium batteries are considered market competitors in the future.[5] However, high operational temperatures can cause severe damage to their liquid system and electrolyte, limiting their industrial application. Furthermore, sodium batteries demonstrate a promising performance for the storage of renewable energy from solar cells, power grids and electric vehicles given that they safely work at a higher temperature and have lower air sensitivity compared to lithium.[8] Gratifyingly, the research on achieving an operational battery temperature in the intermediate position is ongoing with various modifications and several changes already applied for battery system improvement.[9] The main disadvantages associated with sodium batteries are their low energy density, low cyclic stability and operational temperature, which are also a major area of research and further improvements are needed. Moreover, considering the advancement of battery technology to achieve ultrafast charging (80% charge within 5 min), the recyclability of cathode materials has been proposed recently. Hence, we need to focus on the recyclability and higher cyclability of the components of sodium batteries for their industrialization.[10]

In Na-batteries, Na-metal is used as the anode material, while the cathode is generally a higher surface carbon, liquid sulphur or a layered oxide material.[11] Besides, the medium, electrolyte, electrolyte additive, highest occupied molecular orbital (HOMO) and lowest unoccupied molecular orbital (LUMO) energy gap of the electrolyte and additive, cathode and anode materials, electrolyte viscosity, and temperature are the key factors affecting the performance of sodium batteries.[11] Presently, although the aqueous sodium battery is a low-cost market option, its narrow operational window limits its usefulness. Hence, organic electrolytes are comparatively better suited to achieve a high specific capacity.[12] Recent studies focused on the improvement of doping in the inner side of the core, increasing the porosity of carbon materials, and using a high-conductive electrolyte to *in situ* engineer the material.[1] Doping can also increase the electron density at the metal sites, which will enhance the storage of ions in both the cathode and anode. Moreover, the construction of the cathode and anode with different hard carbons enhances the Na storage performance. Initially, Prussian-based materials were used as the cathode material for sodium storage; however, the negative ion material does not provide stable structure.[13] Hence, further design is needed for the application of sodium batteries. In this case, the rational design of the yolk–shell structure enables the controlled growth of the shell and core structures, where the void between shell and core can facilitate the Na^+ insertion/extraction process, which are systematically synthesized by controlling the ratio of the precursor reagents.[14]

Sodium-ion batteries involve mainly three mechanistic pathways, *i.e.*, charge insertion mechanisms for intercalation, alloying, and conversion.[15] The term ''insertion'' has also been employed to describe the introduction of foreign species (atoms, ions, and molecules) into the host lattice.[15] Furthermore, the term intercalation is used in batteries, which is also one type of topographical insertion of a guest molecule in batteries. The term intercalation is associated with major structural changes during the alloying possess, *i.e.* a sodium ion is intercalated in the host lattice by insertion as a guest molecule. The significant difference between insertion and intercalation involves volume changes.[15] In the case of the intercalation process, large-size sodium ions cause volume changes, which create a higher activation energy as a result of loss of capacity. Besides the intercalation method, alloying is another widely investigated process, where Na^+ ions are inserted into the host matrix and form an alloy-based compound.

The importance of the alloying reaction is a lower cell voltage operation with higher gravimetric capacity compared to the intercalation process.[15] However, higher mechanical stress and loss of electrical contact are the critical drawbacks of this process. Hence, several improvements in the alloying

Anurupa Maiti

Dr Anurupa Maiti obtained her bachelor's degree from Vidyasagar University, India, and PhD from the Indian Institute of Technology Kharagpur, in 2022. Following her doctoral studies, she conducted postdoctoral research at the Indian Institute of Science Education and Research, Kolkata. In addition to her research endeavors, Dr Maiti has pursued a PG-Diploma in Machine Learning, showcasing her multidisciplinary interests. Her research focuses on electrochemistry, particularly in the realm of organic electrocatalysis, coupled with applications of machine learning. This combination of expertise suggests a forward-looking approach to tackling challenges at the intersection of chemistry and data science.

process are extensively demanded.[16] The main issues are related to large volume expansions, typical voltage hysteresis during discharging cycles and sluggish energy storage process.[17] The LUMO and the HOMO energy gap of the electrolyte in SIBs determines their thermodynamic stability window.[18] The critical issue of Na-ion batteries is the degradation of their performance at low temperatures below 0 °C, where the Na^+ ion loses its diffusion ability and at higher temperature, which is not applicable for EV application due to safety concerns.[19] Hence, a wide operation temperature range should be the focus of future research for the commercialization of SIBs. In this case, several chemical modifications such as heteroatom doping[20] and formation of composites and covalent networks have been applied, but there is a long way to go to achieve the target values for industrialization processes like lithium batteries.[15] Furthermore, to compete in the commercial market with Li-ion batteries, some challenging drawbacks arising from SIBs have to be addressed. The construction of Na-ion batteries with a low-temperature range, Na^+ migration, and higher operational voltage should be controlled to achieve the maximum performance.[19] In general, the SIB electrolytes are a mixture of organic electrolytes with dissolved sodium salts. However, the organic electrolytes utilized for SIBs are linear/cyclic carbonates and ethers of non-degradable sodium salts. The electrolyte is prepared by mixing 1.0 M of $NaClO_4$ or $NaPF_6$ salt in ethylene carbonate (EC), propylene carbonate (PC), dimethyl carbonate (DMC), diethyl carbonate (DEC), and ethyl methyl carbonate (EMC) solvents.[21]

Yolk–shell structures have been rationally designed due to their capability to alleviate volume expansion and accumulate numerous ions in their cavity.[22] In general, a yolk–shell structure has a suitable void space to facilitate electron transfer and its co-tuneable phases can enhance the rate capability of sodium storage. The scalable and easily accessible methods for the preparation of yolk–shell structures provide diffusion channels, which also influence their sodium storage capacity.[23] The synthesized yolk–shell structures provide a shorter Li^+/Na^+ diffusion distance and enhance the penetration of ions in the anode or cathode.[24] Also, the integration of a carbon shell on yolk–shell structures prevents corrosion from the electrolyte and improves the conductivity of the materials. Furthermore, any undesirable reactions are completely disrupted from the electrolyte by the protective shell structures. The controlled synthesis of yolk–shell structures can tune their thickness, size, and shell volume, which is capable of regulating their sodium storage performances.[25] In addition, the integration of yolk–shell structures affects the dielectric constant, conductivity and penetration of the electrolyte. The design of scalable yolk–shell structures requires low-cost equipment with a setup to achieve a wide range of temperatures.[26] Yolk–shell structures integrated with conducting carbon shells increase the rate capability and cycle stability. Further, although microspheres, flakes, flowers, and 2D layered structures are also attractive for application in SIBs, the recent literature suggests that yolk–shell/core shell structures with different morphologies can achieve the maximum practical significance.[27] Recent developments in the low-cost synthesis of core–shell structures also demonstrate the facile integration of electrode materials. Although a comparative overview provides insight into the mechanism, it depends on the material design, conductive platform, mesoporous channel, *etc.* Core–shell and yolk–shell materials enhance the reversible capacity, battery cyclability, rate capacity and lifetime in comparison to other nanomaterials.[28–30] The void of the yolk aids the growth of a stable SEI layer on the carbon shell, and hence increases the cycle stability.[31] The carbon shell also stops the pulverization of the core and stops the volume expansion during cycling.[31] Moreover, the multi-shell core or yolk shell structure enhances the synergistic effect and maintains long-term interaction.[32] Hence, by changing the reaction conditions, solvent ratio and surface integration, the performances can be maximized. The notable cycle stability of yolk–shell and hollow core–shell structures is slightly higher compared to core–shell structures. Thus, this review comprehensively discusses the design of yolk–shell and core–shell structures, their controllable parameters, and surface integration. Importantly, the related commercialization of lithium-ion batteries and sodium-ion batteries and recent topics of machine learning on batteries are also discussed. The synthetic procedures and role of yolk–shell/core–shell structures across wide electrochemical applications are proposed in the critical discussion. Finally, a summary of our critical views on sodium batteries are presented in the last section.

2. Effects controlling the sodium storage performances

According to recent research, various cathode materials in SIBs such as Na-based layered oxides,[33] sodium superionic conductor materials[34] and fluorophosphates,[35] have attracted considerable attraction. However, the major challenge associated with these cathode materials is their close-packed oxygen ion array, which hinders the diffusion of sodium ions.[29] However, the future modification of cathode materials can enable high sodium ion storage, long life, and high rate capability.[30] Although layered rock salt structures have been shown to be promising materials for sodium storage due to their intercalation property, they show poor cycle stability due to their volume expansion during the alloying reaction.[36]

Again, doping can maximize the reversible capacity by improving the reactivity at the surface/interface region by reducing the solid electrolyte interfacial resistance.[37] Doping causes a reduction in the kinetic barrier of Na^+ ion movement in the intrinsic structure. Moreover, a higher quantity of dopant can control the cyclability and rate capacity performance.[38] Doping of nitrogen atoms in FeS_2/Fe_3O_4@C,[39] yolk-like TiO_2,[38] $MoSe_2$-C,[40] and Bi_2S_3@mesoporous carbon[41] nanocomposites resulted in a higher reversible capacity. Furthermore, introducing a higher degree of pyrrolic nitrogen,[42] multi-metal interaction[43] promotes the reversible capacity and rate capacity.[44] Covalent assembly with inorganic materials also

facilitates the ion diffusion kinetics, outstanding mechanical stability and interlayer electron transfer.[45] Moreover, a hierarchical porous structure facilitates the charge transfer kinetics and acceleration of electrolyte transport, which improve the reaction kinetics.[46] Covalent triazine frameworks as facile and low-cost synthesized networks deliver a high reversible capacity due to their two-dimensional exfoliated few-layered structure.[47] A coating of carbon layer also regulates the superior sodium storage performances.[48] A recent investigation also showed that a carbon coating on the cathode and anode increases the conductivity of their materials and increases their performances.[49] The optimum void space also accumulates charge, exhibiting the best cyclic performances.[50] It was found that a nano-size (~15 nm) pore diameter could sustain over 80% capacity retention during 1300 cycles at 5 A g^{-1}.[51] However, it was observed that 10–20 nm carbon layer and pore volume of around 10 nm resulted in a capacity of 198 mA h g^{-1} at 20 A g^{-1} over 10 000 cycles.[50] It was also noticed that a yolk size of ~100–200 nm and carbon thickness of 20 nm with the average pore radius of 2 nm resulted in 90.8% capacity retention after 1000 cycles at 1 A g^{-1}.[52] Hence, it is preferable to maintain the pore size of 10 nm to obtain a higher electrochemical performance. Moreover, the optimum hollow structure can prevent large volume expansion and enhance the electronic conductivity, which also result in an enhancement in stability and rate capability.[53,54]

Researchers developed a new electrospinning technique for SIB application, where a large surface area and high porosity could be obtained.[55] Additionally, the defective carbon material prepared through the electrospinning method also resulted in an increase in the reversible capacity.[56] It has also been noted that crystalline materials in regular form show higher intercalation of sodium ions through their regular plane. The preferential orientation of the (102) and (104) facets of layered oxides could improve the capacity and rate performance.[57] Furthermore, the ball-milling process increased the ionic conductivity of the material compared to the materials synthesized *via* other methods, where the tetragonal form provides a greater capacity than the cubic form.[58] Recent advances showed that the anode material in sodium batteries is very important in controlling their reversible capacity and cycle stability. The electrode using the standard poly(vinylidene difluoride) binder exhibits the weakest electrochemical properties, while that employing sodium alginate binder supplies the best reversible capacity and higher cycle stability with higher capacity retention due to its high ionic conductivity.[59] The SIB electrolyte also enhances the capacity by regulating the solvent and salt concentrations.[60] For industrialisation, a bulk amount of materials is needed for their proper application. Among the synthesis methods, the spray drying method is the one of the facile, simple methods for large-scale production.[61] The proper choice of the substrate for the current collector also has a great impact on the performance of SIBs. Among the foils, aluminium foil is a low-cost material, simple, and easily synthesized as the current collector.[62] The standardization of anode materials can also potentially impact the storage performances of SIBs. Among the anode materials, sulphides, phosphides, selenides, and nitrides are used due to their high storage capacity in SIBs.[63–65] A recent investigation showed that phosphide materials offer several advantages such as higher energy density and superior kinetics.[66] Among the phosphorus materials, black phosphorus shows the highest reversible capacity and lowest ion diffusion coefficient.[67] Further, ultra-stable cycle performances can be controlled by tuning the thickness of the material.[68] Morphology construction is another vital parameter for regulating the storage capacity. In this case, compared to hierarchal micropore structures, hollow urchin-type structures showed a higher reversible capacitance due to their adjustable porous channels and void space.[69] Moreover, 2D graphene-based compounds with abundant oxygen-containing functional moieties facilitate the storage of sodium ions. The honeycomb-like structure is one of the structures that promotes the sodium ion storage capacity, which is favourable for a high sodium storage capacity.[70] The voltage window is another factor for improving the capacity. A literature study showed that an anode material containing redox pairs exhibiting a voltage plateau at 3.4 V (*vs.* Na^+/Na) in the range of 1.0–4.0 V delivered a higher reversible capacity but inferior cycling stability.[71] Also, to overcome safety issues such as membrane damage and flammable liquids, well-designed and modified membranes have been engineered recently.[72] A polymeric electrolyte membrane such as PFSA-Na showed high ionic conductivity, outstanding thermal stability, and excellent mechanical flexibility in a wide temperature range.[73] The charge–discharge capacity and coulombic efficiency also depend on the electrolyte. It was noted that a polymeric gel electrolyte containing polyvinylidene fluoride-hexafluoropropylene (PVDF-HFP) resulted in a higher coulombic efficiency.[74]

3. Yolk shell and core shell

Yolk–shell NPs consist of a movable core/shell with optimum void or outer shell with the same or different materials. The void space is generated through the removal of the sacrificial layer or partial etching of the outer shell. The inner core or yolk material generally consists of different metals or metal oxides, non-metal oxides, metal sulfides, phosphides, selenides, bimetallic compounds, *etc.*[27,38,43,75] Furthermore, porosity can be introduced in the material by different template etching methods. Core–shell structures consist of a core/sacrificial shell/outer shell structure. Recently, many studies have been reported on yolk shell and core shell structures with different applications.[76,77] Generally, the core consists of an inorganic metal or polymetallic small materials, which is further covered by hard templates such as different carbon and hard templates.[78] The core shell or yolk shell can be synthesized through different template-assisted or template-free methods such as galvanic replacement, Ostwald ripening, and self-assembly methods. These methods are systematically described in the following sections. Fig. 1 depicts the formation of the core and yolk shell structure.

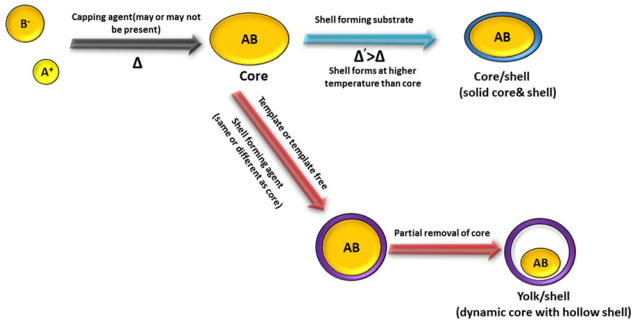

Fig. 1 Schematic representation of the core–shell and yolk–shell structure.

3.1. Synthesis of yolk shell

3.1.1. Template-directed synthesis. Sacrificial template-assisted synthesis is a crucial technique for crafting yolk and core–shell structures, enabling meticulous control of their shape, composition, and properties.[79] This method relies on sacrificial materials, which are strategically eliminated after the synthesis to form void spaces or distinct shell layers. Yolk–shell (YS) nanostructures are comprised of two layers, *i.e.*, an outer shell and an inner yolk and sacrificial template.[28] The sacrificial template functions as a temporary scaffold or framework in manufacturing processes, particularly in the fields of nanotechnology and materials science. It acts as a mold around which the desired structure is fashioned. Once the desired structure is realized, the sacrificial template is extracted, leaving the final product. Sacrificial templates are applied in various synthesis methodologies aimed at achieving specific architectures such as yolk–shell or core–shell structures. These templates can be crafted from materials that readily undergo etching, dissolution, or removal through chemical or physical means without damaging the desired structure.[29,31] In the context of yolk–shell structures, for instance, the sacrificial template forms the inner "yolk" layer, which is selectively eliminated to create void spaces within the outer shell. This procedure allows meticulous control of the morphology and characteristics of the resulting nanostructure. In essence, sacrificial templates play a pivotal role in the precise fabrication of intricate nanomaterials and nanostructures, empowering researchers to tailor properties for a wide array of applications.[79]

Sacrificial templates can be classified as hard and soft templates. Templates such as silica, Fe_3O_4, V_2O_5, Cu_2O, carbon, FeOOH, gold, and AgBr are generally used as hard templates.[80] Silica is a well-known hard template, which is usually removed by hydrofluoric acid or in hot concentrated alkaline/ammonia solution.[81] The etching of silica though HF creates water-soluble H_2SiF_6 due to the high electronegativity of fluorine. The alkali etching process is slightly slower than acid etching and alkali treatment generates soluble sodium silicate. However, the acid etching process requires more safety measures and precaution compared to alkali medium. Notably, the ammonia etching of silica provides a void space of 50 nm in the material. Besides the silica template, several familiar hard templates such as Au/TiO_2,[79] Pd/C,[82] Pd/CeO_2,[83] γ-Fe_2O_3/Y_2O_3,[84] Pd/SiO_2,[85] and Fe_3O_4/SiO_2[86] have been used for the construction of yolk–shell structures. Besides them, many other inorganic sacrificial templates have emerged for synthesis of yolk–shell structures such as V_2O_5,[87] Ni,[88] Cu_2O,[89] and AgBr.[90] Metal salts and metal oxides produce an acid-soluble metal core, which is removed by the dissolution process. In addition, metal hydroxides synthesized by different methods followed by calcination, produce metal oxide-like yolk–shell structures.[91] In general, the removal of any volatile or any chemical product can also produce yolk–shell structures. Further, multi-shell yolk shell structures could be obtained through electrostatic interaction among different structure directing agents with silica. Multi-shell yolk–shell structures were obtained *via* the successive addition of bis(trimethoxysilyl)ethane and TEOS.[92,93] The co-structure-directing agent APTES was attached to the SiO_2 core–shell structure through electrostatic attraction. The thickness of the silica-shell could be controlled by varying the concentration of TEOS as the silica source. Importantly, the partial etching of the core structure produced a yolk–shell structure.[94,95] The Dou group[96] demonstrated the preparation of yolk–shell FeS@carbon nanospheres, which showed a high capacity of approximately 545 mA h g^{-1} over 100 cycles. These nanostructures enabled the Na/FeS@C battery to achieve an ultrahigh energy density of approximately 438 W h kg^{-1}, making them suitable for commercial applications. Their method involved coating Fe_3O_4 nanoparticles with a sacrificial layer of condensed silica using the Stöber method, followed by the addition of resorcinol formaldehyde (RF) *via* the sol–gel process. The resulting Fe_3O_4@C nanospheres underwent a carbonization process through calcination, and the sacrificial silica layer was removed using concentrated NaOH to produce the yolk–shell structure.

In the realm of soft template-based approaches, the synthesis of yolk–shell nanostructures has attracted significant attention. The synthesis of yolk–shell nanostructures involves the complete removal of the soft template through thermal annealing or calcination. However, the void size in the core–shell structure is the most important factor influencing the sodium storage capacity, which allows the active materials to expand easily without damaging the outer protective shell. Further, a too large void space reduces the volumetric energy density.[97] Hence, the desirable thickness of the void should be tailored to obtain a higher reversible capacity and cycling performance.[97] Researchers also used surfactants such as an aqueous mixture of lauryl sulfonate betaine (LSB, a zwitterionic surfactant) and sodium dodecyl benzenesulfonate (SDBS, an anionic surfactant), and Triton X-100 surfactant[98–100] to increase the electrostatic interaction among the precursors. The soft template CTAB in ethylene glycol medium produced microsphere structures and yolk–shell structures were obtained after the acid etching process.[101] F127 is another important fluorocarbon surfactant, which electrostatically interacts with the core particles to generate mesostructures after the subjecting them to calcination.[102] In addition, sulfur serves as a sacrificial template for yolk–shell nanostructures. The sulfur

core can be dissolved in various organic solvents, including toluene, carbon disulfide, xylene, carbon tetrachloride, and benzene.[103] Furthermore, the sulfur core template can also be eliminated by increasing the calcination temperature. In the case of the sacrificial template, silver can be removed by employing a dissolved NH_3 solution, resulting in the formation of a silver amine complex.[104] Additionally, β-FeOOH nanosheets served as a sacrificial template, which could be fully reduced to Fe_3O_4.[105] A mixture of two oxide or nitrate salts in concentrated sodium hydroxide solution also produced yolk–shell structures.[106] In summary, yolk–shell synthesis involves intricate control of the sacrificial templates, etching processes, and precursor addition to achieve the desired void spaces, which are crucial for high-performance applications such as energy storage systems. However, sacrificial templates are associated with high cost and achieving integral yolk–shell structures with the desired morphology can be challenging. Additionally, the removal of the template can present difficulties, adding to the complexity of the process. In the case of hard templates such as silica, their removal involves chemical processes such as etching. Alternatively, soft templates are typically removed through thermal annealing or calcination. Further, the void size is important in yolk–shell structures for achieving the optimal performance in applications such as energy storage. Various surfactants and reagents are used to enhance the electrostatic interactions among the precursors and facilitate the removal of the template. Achieving precise control of the sacrificial templates and etching processes is crucial for obtaining the desired void spaces in yolk–shell structures, which are essential for high-performance applications. However, the challenges related to cost, morphology control, and template removal complexity need to be addressed.

3.1.2. Sacrificial carbon templates. Sacrificial carbon templates are used to increase the cycling and rate capacity of electrodes owing to their high electrical and ionic conductivities and mechanical strength.[41,107] In general, the shell–void–core can be treated as a sodium storage reservoir where the sacrificial template generates the hollow-shell after treatment by the partial etching method. Recently, carbon coating has attracted attention due to its large volume expansion and low capacity loss during prolonged cycling.[41] Moreover, carbon coating with a higher surface area and mesopores is still challenging given that pulverization and cracking occur due to the extreme volume expansion.[41] The carbon layer is formed by the calcination process and etched partially by heat treatment. Also, its size can be tuned by adjusting the reaction time, concentration of the carbon precursor, and temperature. Generally, the carbon template layer can be completely or partially detached by calcination at high temperature in the presence of air.[108] It has been noted that carbon ($\geq$30 wt%) coating on the core or yolk increases the cycling stability and rate capability.[78] To date, many yolk–shell nanostructures have been synthesized such as Fe_3O_4/SiO_2,[109] Fe_3O_4/C,[110] SnO_2/C,[111] Au/SiO_2,[112] Fe_2O_3/SiO_2,[113] Sb@C,[114] and Fe_3N@C[115] using a carbon layer as a sacrificial template, which is partially or completely removed by calcination in the presence of air. In many cases, hollow carbon spheres are chosen as the sacrificial template, where the diffusion of the core precursors occurs inside, followed by a coating of shell material outside the carbon layer. Subsequently, heat treatment of the carbon layer generates a yolk–shell nanostructure. The tuneable size of yolk–shell nanostructures can be controlled by tuning the concentration of the carbon precursor, reaction time, and temperature. In general, organic compounds such as glucose[109,116] and urea[117] can also be carbonized under hydrothermal conditions.[112,118,119] In general, a polymer layer is synthesized as a sacrificial template for the design of yolk–shell nanostructures. Subsequently, calcination and dissolution in appropriate solvent techniques are applied for the removal of the sacrificial layers.[108] The outer shell of the yolk–shell structure can also be derived from an MOF structure.[120] Many yolk–shells are prepared by using templates (brackets) such as silica/silica/(polystyrene),[121] SiO_2/TiO_2/(polystyrene),[122] TiO_2/SiO_2/(poly(methacrylic acid)),[123] Fe_3O_4/SiO_2/(poly(*N*,*N*′-methylenebisacrylamide-*co*-methacrylic acid))/(poly(methacrylic acid))[124] and silica/divinylbenzene-*co*-methacrylic acid (PMAA).[125] Generally, the synthesized carbon layer is a water-soluble precursor, which can be removed by dehydration, polymerization, condensation, and carbonization steps. Upon hydrothermal treatment, carbonaceous-shells are obtained by hydronium ions in acidic pH or by the degradation of the organic compounds. Furthermore, as the carbon template, polyvinylpyrrolidone (PVP) and polyethylene glycol templates can also be used for the preparation of yolk–shell structures.[126] Furthermore, a rigid carbon shell was beneficial for the growth of the SEI layer and prevent the aggregation of the core particles.[127] PVDF is also utilized as a carbon material, which upon pulverization at 600 °C exhibits a high surface area.[126] In addition, after etching with hydrochloric acid, a dopamine-treated carbon-shell showed a much higher surface area. The Sun group synthesized hollow multi-layer mesoporous carbon spheres as a carbon-shell from dopamine by treatment with 4 M hydrochloric acid, which showed a surface area of 1546.76 $m^2\ g^{-1}$.[40] Shen and co-workers prepared tin phosphides@carbon as a yolk–shell structure, where dopamine hydrochloride constructed the carbon-shell, showing a surface area of 128.6 $m^2\ g^{-1}$.[128] The calcination of polypyrrole and polydopamine microspheres also produced a carbon-shell with a higher surface area.[129] Phenolic resin (RF) is the another sacrificial coating that produces a higher surface area. The Yu group prepared Bi@Void@C nanospheres derived from phenolic resin, which exhibited a significantly higher surface area of 168.9 $m^2\ g^{-1}$.[50] Moreover, the Ji group prepared yolk-like TiO_2 with carbon as a shell synthesized *via* the Ostwald ripening method, exhibiting a higher specific surface area of 144.9 $m^2\ g^{-1}$, which is suitable for sodium storage capacity.[130] In summary, the use of sacrificial carbon templates can enhance the cycling and rate capacity of electrodes, particularly in the context of yolk–shell nanostructures. These templates serve as reservoirs for sodium storage, generating hollow shells through partial etching methods. Carbon coating has attracted attention due to its ability to accommodate volume expansion and minimize capacity loss during cycling, although challenges such as

Table 1 Summary of electrochemical performances of yolk shell structures using sacrificial carbon as a template

Materials	Current density (A g^{-1})	Capacity	Cycle	Template	Capacity retention	Ref.
FeS/C	0.1	300.4 mA h g^{-1}	10 000	Iron naphthenate and mercaptoethanol	81.1% after 10 000 cycles	27
NC TiO_2-Y	20C	115.9 mA h g^{-1}	—	Diethylenetriamine		38
$SnSe_2$/$NiSe_2$@NC	3	322.7 mA h g^{-1}	7500	Dopamine	—	43
Sb@Void@GDY	1	325 mA h g^{-1}	8000	Hexaethynylbenzene	74% after 8000 cycles	28
Co_3O_4-C	0.5	311 mA h g^{-1}	200	Polyvinylpyrilidone		31
FeS_2@C	0.1	511 mA h g^{-1}	100	Polydopamine	—	29
CoSe/C	16	361.9 mA h g^{-1}	—	ZIF-67	—	131
Fe_3N@C	2	248 mA h g^{-1}	300	Polyacrylonitrile	—	132
CoS_2/VS_4@NC	5	417.28 mA h g^{-1}	700	ZIF-67	—	32
ZnS@C	1	211.1 mA h g^{-1}	5700	CTAB	—	133

pulverization and cracking persist. Control of the size of yolk–shell structures is achieved by adjusting the reaction parameters. Various materials, including organic compounds and polymers, serve as sacrificial templates, with their removal accomplished through calcination or dissolution. Additionally, carbon templates can facilitate the growth of the solid electrolyte interphase (SEI) layer and prevent particle aggregation. Further, yolk–shell structures using carbon templates derived from dopamine and phenolic resin, among others, can achieve high surface areas conducive to sodium storage capacity. However, despite their scalability and high porosity, challenges remain, including template removal and multistep complexation process. Table 1 shows some electrochemical performances using sacrificial carbon as a template in the preparation of yolk shell structures.

3.2. Galvanic replacement

Galvanic displacement is a simple, low-cost, facile technique, where room temperature stirring of the reactants produces high exposed edges and facets in yolk shell structures.[134] Galvanic replacement reactions lead to a controllable size, shape, hollow interior, and different morphologies using a sacrificial template, where two different electrochemical potentials provide yolk–shell nanostructures.[135] Generally, the lower standard reduction potential material is treated as the sacrificial layer and the higher standard electrode potential metal is used as the shell. For example, when a copper strip was immersed into a higher reduction potential silver nitrate salt solution (Ag^+/Ag), the copper strip is gradually corroded in the solution as Cu^{2+}. Hence, some of the exposed sites of the copper are deposited on the Ag crystal and replace some Ag atoms.[135] In the galvanic replacement reaction, a seed growth reagent such as CTAB and PVP is needed for metal growth and a higher reduction potential metal salt solution is prepared for seed growth.[135] The hollow core is chosen as a presynthesized template such as any lower reduction potential microsphere, nanocage, and nanobox.[136] As the reaction gradually proceeds, the different presynthesized template morphologies gradually dissolved and co-deposited with the higher reduction potential material. The galvanic replacement reaction also occurs with non-metallic solutions such as sulphur and selenium. Here, excess non-metallic solution is used as the template upon which metal is nucleated and excess nonmetal is further removed by choosing the appropriate solvent.[137] Several studies reported that an anti-galvanic reaction may also occur if the size of the higher reduction material such as Au is used less than 3 nm, and then it can reduce the lower reduction potential Ag^+.[138] Further, the alkali medium of the salt solution may favour the multi-shell core–shell structure compared to aqueous medium.[138] The shell thickness and voids are also regulated by galvanic replacement. This strategy can be utilized to prepare different types of multi-shell-alloy. The Xia group prepared yolk–shell structure Pd@Au_xCu_{1-x} yolk–shell nanocages where Pd@Cu core–shell nano-cubes were placed in solutions of $HAuCl_4$.[139] Tao and co-workers synthesized Au@AgPd nanoparticles, where the pre-synthesized Au@Ag core shell was treated with Pd^{2+} ions. Subsequently, galvanic replacement of silver by Pd produced open-mouth yolk–shell-type structures (Fig. 2).[139,140] This galvanic replacement was further modified by the Kirkendall effect. This Kirkendall effect has been designated as a classical phenomenon where diffusion occurs at the interface between two metals with different mobility. The Kirkendall effect is a similar phenomenon to galvanic replacement, where the higher diffusion coefficient metal provides a higher vacancy flux, while the lower diffusion

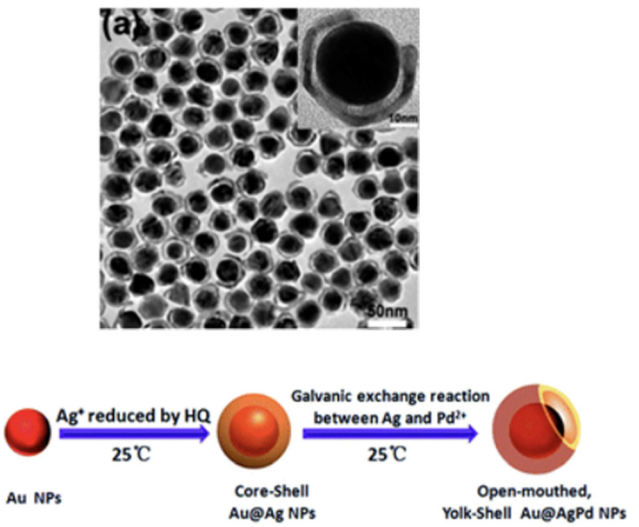

Fig. 2 (a) Low-magnification TEM image (a) of OM-YS Au@AgPd NPs and schematic representation of the synthetic procedure for open-mouthed, yolk–shell Au@AgPd NPs *via* the galvanic reaction of Au@Ag NPs with Pd^{2+} ions at room temperature. Reprinted with permission from ref. 140. ©2015, the Royal Society of Chemistry.

Table 2 Summary of electrochemical performances of yolk shell structures prepared using galvanic replacement

Materials	Current density	Capacity	Cycle	Capacity retention	Energy density (W h kg^{-1})	Method	Ref.
Sb NTs	1 A g^{-1}	342 mA h g^{-1}	6000	74% @6000	252	Galvanic replacement	146
Sb@C@TiO_2	1 A g^{-1}	193 mA h g^{-1}	4000	67% after 400 cycles	179	Galvanic replacement	147
Sb/TiO_2	2 A g^{-1}	245 mA h g^{-1}	—	87% after 100 cycles	—	Galvanic replacement	148
Sb⊂CTHNs	0.1 A g^{-1}	607.2 mA h g^{-1}	100	—	—	Galvanic replacement	149

coefficient material provides less vacancy. The different vacancy flux creates a yolk–shell structure. The excess vacancies near the higher diffusion coefficient are called 'Kirkendall voids'. The Kirkendall effect occurs if atomic diffusion occurs *via* vacancies and each component possesses different mobility.[141] A hollow-shell is created by oxidation, phosphidation, or chalcogenation through the Kirkendall process. Various composites such as Sn@void@SnO/SnO_2, FePt@Fe_2O_3, and Au/Fe_2O_3 have been prepared through the Kirkendall effect.[142–144] In 2013, the Oh group[145] developed a unique galvanic replacement process, where pre-synthesized square prism-shaped Mn_3O_4 nanocrystals (~20 nm) were kept in an iron(II) perchlorate solution. It was observed that the ionic Fe^{2+} gradually underwent oxidative precipitation to form Fe_2O_3, while Mn(III) was reduced to Mn(II) and dissolved in the reaction mixture. Hence, the Fe_2O_3 slowly replaced some of the Mn(III) and deposited on the Mn_3O_4 nanocrystals. Upon increasing the concentration of iron(II) perchlorate, the size of the hollow interior increased. They showed that the presence of clear facet-like structures in the FFT spot pattern of the exposed nanocage-like γ-Fe_2O_3 structures. This exposed nanocage-like structure exhibited superior lithium storage compared to other materials.[145] Galvanic replacement is very simple and cost effective but its complexity, long reaction time, scalability, purity and diffusion control of ions make its application in batteries. Table 2 presents a summary of the different materials prepared through galvanic replacement reaction towards SIB application. In summary, galvanic displacement is a straightforward and cost-effective method for producing yolk–shell structures with high exposed edges and facets. It involves a controlled reaction between two different electrochemical potentials, typically using a lower standard reduction potential material as the sacrificial layer and a higher standard electrode potential metal as the shell. Seed growth reagents aid in metal growth, and presynthesized templates dictate the hollow core morphology. This process can also occur with non-metallic solutions such as sulfur or selenium. Galvanic replacement, often modified by the Kirkendall effect, allows the regulation of the shell thickness and voids, and the creation of multi-shell alloys. However, although it is simple and cost-effective, challenges in terms of scalability, purity, and ion diffusion control hinder its application in battery technology. Table 2 shows some electrochemical performances using galvanic replacement for the preparation of yolk shell structures.

3.3. Ostwald ripening

Ostwald ripening refers to the creation of yolk–shell structures using the solubility property of crystal aggregations. This process is based on the Gibbs–Thomson influence, which facilitates the growth of larger particles, and the dissolution of unstable smaller particles with a critical size (Fig. 3).[150] In this process, larger nanoparticles break into smaller ones and aggregate to form a larger core molecule, which possesses shell molecules. The small molecules aggregate to the centre to create a spherical aggregate. Yolk–shell nanostructures have been synthesized *via* symmetric and asymmetric aggregation, where small nanoparticles aggregate around the solid spheres. These small crystallites are dissolved during the recrystallization to make the void space move towards the outer shell, while their movable core part consists of solid spheres.[151,152]

Generally, this method is the most common strategy to generate hollow materials. In this process, generally, a solvent mixture upon long-term hydrothermal treatment without the addition of any template generates mesoporous-like structures. The surface area varies from 110–150 m^2 g^{-1} and the extra void space is capable of accommodating the lithium atom in its structure.[153] The Ostwald ripening method is the best-suited method for generating hollow mesoporous materials compared to other methods given that it does not involve the use of hazardous chemicals. The α-Fe_2O_3/SnO_2 yolk–shell structure was synthesized by the Ostwald ripening mechanism, where the SnO_2 nanoparticles were prepared from $K_2SnO_3{\cdot}3H_2O$ and deposited around the α-Fe_2O_3 NPs. Here, the hydrothermal treatment of SnO_2 nanoparticles resulted in their dissolution and created a void space.[154] Researchers also employed template-free Ostwald ripening processes for the synthesis of Fe_3O_4/Co_3O_4,[155] Pt/CeO_2,[91] and Au/Cu_2O[156] nanostructures. The Bao group summarized the Ostwald ripening process for

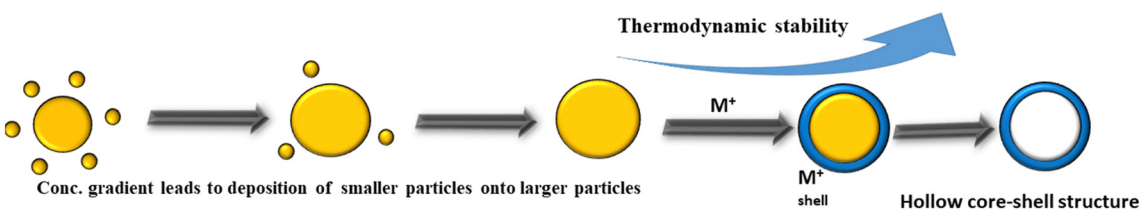

Fig. 3 Schematic design of Ostwald ripening.

the preparation of materials for the fabrication of lithium-ion batteries, where solid TiO_2 spheres, VO_2 hollow microspheres, MnO_2 hollow structures, and Fe_3O_4 hollow nanospheres were prepared by treating their metal salt by the hydrolysis method or heating in the hydrothermal method.[157] Often, the polarity of the solvent also increases the yield of the materials. The Zhaou group demonstrated the synthesis of $Na_3V_2(PO_4)_2O_2F$ (NVPF) by Ostwald ripening, where larger nanoparticles produced the shell with several inner nanospaces and pores under solvothermal conditions. This material demonstrated exceptional cycling stability (0.023% capacity decay per cycle after 2000 cycles at 20C).[158] Park and co-workers synthesized a goat pupil-like configuration of S-doped SnSe yolks and hollow carbon shells through the Ostwald ripening method, which also showed excellent cycle stability.[159] Later, the same group showed the generation of Co_3O_4-C hollow yolk–shell through the Ostwald ripening method for super performances towards lithium and sodium batteries.[31] Zhang *et al.* also prepared yolk-like TiO_2 through the Ostwald ripening method, which showed a high rate capability.[38] The template-free approach using Ostwald ripening can potentially offer advantages such as simplicity, reduced cost, and scalability compared to methods involving the use of external templates. However, optimizing the process parameters and understanding the underlying mechanisms of Ostwald ripening are crucial for achieving the desired nanostructure characteristics and properties. In summary, Ostwald ripening is a method for creating yolk–shell structures by leveraging the solubility properties of crystal aggregations, driven by the Gibbs–Thomson influence. This method can be used for SIB application given that it is a very straightforward reaction for yolk shell production. Table 3 shows a summary of the electrochemical performances of yolk shell structures using Ostwald ripening.

3.4. Ultrasonic spray pyrolysis (USP)

Ultrasonic spray pyrolysis (USP) is a scalable continuous one-step approach for the synthesis of hollow- and yolk–shell nanostructures *via* the decomposition and evaporation method. This process involves the creation of an aerosol (liquid–gas interface) from a liquid precursor solution, which is subsequently transformed into micro-droplets. The micro-droplets are transported into a furnace *via* a gas flow. Inside the furnace, decomposition of the precursor and solvent evaporation occur, leading to the formation of yolk–shell nanostructures. The volatile organic compounds evaporate during the heating process, leaving behind void spaces and resulting in the formation of a yolk–shell structure. Firstly, micro-droplets are generated using USP, followed by evaporation of the solvent. The Suslick group reported the synthesis of a composite using $(NH_4)_2MoS_4$ and silica as the precursors in a liquid, which was then ultrasonically nebulized into microdroplets, carried by a gas flow into a furnace, where the precursor underwent decomposition to create the SiO_2/MoS_2 composite. After treatment with HF, a porous MoS_2 network was obtained, where the surface area and porosity were controlled by the precursor solution.[161] The same group[162] published a study using a Sunbeam model 696, 1.7 MHz, where a household ultrasonic humidifier ($<$\$30) was utilized to conduct the ultrasonic spray pyrolysis method. Silica colloid, styrene, ethylene glycol methacrylate, AIBN and $Co_2(CO)_8$ were used as the template and metal precursors. In this process, SDS was used as the surfactant. The solution was first nebulized into an inert gas stream, which carried the resulting droplets into the first furnace (200 °C), where the solvent evaporated, and the organic monomer polymerized. Subsequently, the resulting solution was fed to the hotter furnace (700 °C), where the fully pyrolyzed organic polymer produced porosity. However, the conversion of this process required 6–8 h and the obtained yield was 40%. The surface area was also likely to be around 200 $m^2\ g^{-1}$.[162] Further, without the use of a template, ultrasonic pyrolysis results in a very low surface. Mai *et al.*[163] reported the preparation of yolk–shell-structured anatase TiO_2 microspheres, where titanium(IV) bis(ammonium lactato)dihydroxide (TiBALDH) and sucrose were used as the precursor solution, which was fed into an ultrasonic atomizer. The black product after treatment in a tube furnace at 600 °C for 5 h in air produced yolk–shell TiO_2 microspheres.[163] Herein, Fig. 4 shows the ultrasonic pyrolysis technique, where titanium(IV) bis(ammonium lactato)dihydroxide and sucrose in water was used as the precursor solution. Here, the TiO_{2-x} microspheres prepared *via* the facile spray-pyrolysis showed remarkable long-term cycling stability.[163] In general, for SIB application, titanium/nickel or iron prepared *via* the spray pyrolysis method have been found to be promising materials.[164] The ultrasonic pyrolysis method is indeed scalable and versatile. However, it also has certain limitations, such as the high cost and complexity of the required instrumentation, as well as challenges related to the preparation and compatibility of the precursors. These factors make it disadvantageous compared to other synthesis methods. In summary, ultrasonic spray pyrolysis (USP) is a scalable method for the synthesis of yolk–shell nanostructures, involving precursor nebulization, decomposition in a furnace, and solvent evaporation. It offers versatility but has limitations including high equipment cost and complexity, with titanium-based materials

Table 3 Summary of electrochemical performances of yolk–shell structures using Ostwald ripening

Materials	Current density	Capacity (mA h g^{-1})	Cycle	Method	Capacity retention	Ref.
NC TiO_2-Y	1C	200.7	550	Ostwald ripening	95.5% after 3000 cycles	38
Co/(NiCo)Se_2	0.2 A g^{-1}	—	80	Ostwald ripening	96% after 10th cycles	160
$Na_3V_2(PO_4)_2O_2F$	50C	85.4	—	Ostwald ripening	84% after 200 cycles	158
Co_3O_4–C	2 A g^{-1}	619	400	Ostwald ripening	—	31
S-doped SnSe	0.5 A g^{-1}	186	1000	Ostwald ripening	74% after 2nd cycle	159

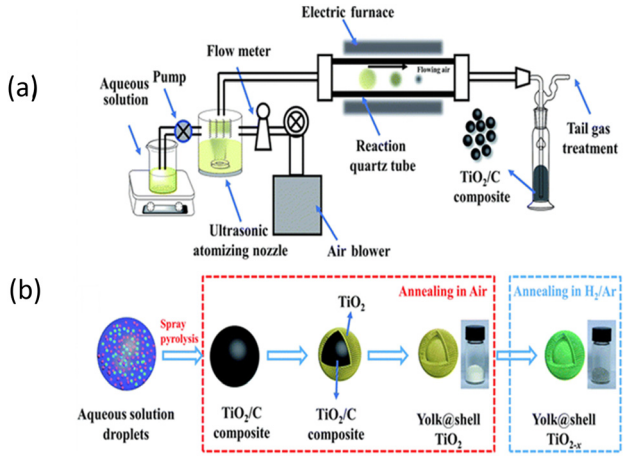

Fig. 4 Schematic diagram of (a) ultrasonic spray pyrolysis process and (b) mechanism of yolk@shell-structured TiO_{2-x} prepared using the ultrasonic pyrolysis method. Reprinted with permission from ref. 163. Copyright: 2019, the Royal Society of Chemistry.

showing promise for sodium-ion battery applications. Table 4 presents a summary of the electrochemical performances of yolk shell structures prepared *via* the ultrasonic spray pyrolysis process.

3.5. The ship-in-bottle method

The Ostwald ripening or galvanic replacement process and Kirkendall effect-based methods have some disadvantages such as low efficiency given that the cores are captured inside shells.[169] Many researchers have employed the "ship-in-bottle" approach for synthesizing yolk–shell nanostructures, wherein the core materials are protected by a mesoporous silica and/or zeolite-like framework. In material synthesis, particularly in nanotechnology, various methods are utilized to encapsulate or confine nanoparticles or nanostructures within a matrix or shell.[170] Subsequently, these encapsulated entities are added in very small amounts into ship-like materials such as zeolites and metal–organic frameworks. The main driving force of this reaction is the electrostatic interaction between the porous template and the small nanoparticles, which are impregnated within the cavity and have dimensions smaller than the pore size of the cavity. In this method, porous templates such as zeolites, MCM-41, metal–organic frameworks, and (SAB)-16 are utilized as hosts to entrap the core particles.[171] Numerous small nanoparticles are encaged *via* the self-assembly method through a chemical reaction in a porous cavity, forming a core-like structure. Various yolk–shell nanostructures such as Fe_2O_3/silica,[172] Pt/silica,[173] and SnO_2/SiO_2,[174] have been prepared *via* the ship-in-bottle process. Likewise, Liu *et al.* prepared MOF crystals for creating porous channels to entrap various small nanoparticles.[170] In the mesoporous UiO-66-NH_2 MOF, nitric acid treatment created a hole in the centre-entrapped palladium salt (Na_2PdCl_4) in the cavity.[170] The Qiu group also used zeolites, where the ions were assembled into the cavity by the ship-in-bottled method.[170] Huang and co-workers[175] synthesized new intermetallic NPs encapsulated with mesoporous silica *via* an easy facile method in the lab. However, intermetallic materials such as Pt–Sn and Pt–Cu could not be synthesized at higher temperature given that it affected their crystal structure. Hence, a silica template was chosen, where silica protected the intermetallic core during heat treatment. Firstly, they mixed 10 mM K_2PtCl_4 and tetradecyltrimethylammonium bromide in distilled water solution. Subsequently, 500 mM (3 mL) aqueous solution of sodium borohydride ($NaBH_4$) was added to the clear solution of the resulting mixture and stirring continued for 15–20 h. The resultant dark brown colloidal solution of Pt nanoparticles was added to a sodium hydroxide solution, where the pH was kept between 11 and 12. While stirring, 500 μL of a 10% tetraethyl orthosilicate solution in methanol was added dropwise. After 24 h, the sample was centrifuged, and the coated particles ($Pt@mSiO_2$) were redispersed in methanol. The surfactant was removed *via* an acidic methanol refluxing (6% hydrochloric acid solution) at 90 °C for 24 h.[175] Sometimes, the cavity of porous carbon is also used for entrapping nanoparticles. Luo *et al.* reported the preparation of flower-like MoS_{2-x} nanosheets (Fig. 5) confined with a carbon layer *via* the ship-in-bottle method, where the cavity of carbon was used as a closed space for reactants, which showed 85.2% capacity retention after 100 cycles.[176] Table 5 presents some of the performances obtained through the ship-in-bottle method. The "ship-in-bottle" method involves encapsulating nanoparticles within a porous template such as zeolites and MOFs. It enables the synthesis of yolk–shell nanostructures, offering protection of the core materials during reactions. Various nanoparticles have been entrapped using this approach, demonstrating promising performances in different applications.

3.6. Core shell synthesis

3.6.1. Sol gel method. The sol–gel technique is versatile and easily scalable, making it suitable for simple lab-scale operations. Initially, this method was primarily employed for creating mesoporous 3D networks, with silicon dioxide (SiO_2) and titanium dioxide (TiO_2) being the preferred sols. In this

Table 4 Summary of electrochemical performances of yolk shell structures prepared *via* spray pyrolysis

Materials	Current density	Capacity (mA h g^{-1})	Cycle	Capacity retention	Method	Ref.
TiO_{2-x}	0.05 A g^{-1}	230.7	200	91.7% after 1000 cycles	Spray pyrolysis	163
$NiCoSe_2$/CNT	0.2 A g^{-1}	366	10 000	85% after 2nd cycle	Spray pyrolysis	165
$(Fe_{0.5}Ni_{0.5})_9S_8$	1 A g^{-1}	527	100	99% after 2nd cycle	Spray pyrolysis	166
TiO_{2-x}/C	50 mA g^{-1}	249	180	87.2% after 2nd cycle	Spray pyrolysis	167
$FeSe_2$/graphitic carbon	0.2 A g^{-1}	510	200	88% after 2nd cycle	Spray pyrolysis	168

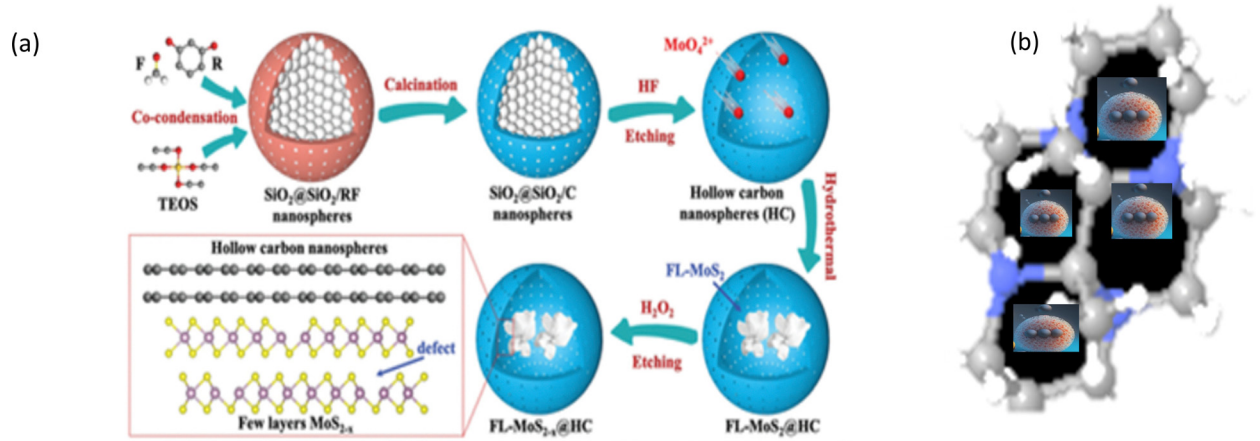

Fig. 5 (a) Illustration of the preparation process of the FL-MoS_{2-x}@HC matrix. (b) Molecular assembly into the molecular porous template. Reprinted with permission from ref. 176. ©2021, Wiley-VCH GmbH.

Table 5 Summary of electrochemical performances of yolk shell structures prepared using the ship-in-bottle method

Materials	Current density	Capacity	Cycle	Method	Capacity retention	Ref.
MnS@C	0.5 A g^{-1}	336 mA h g^{-1}	200 cycles	Ship in bottle	—	177
MoS_{2-x}/C	2 A g^{-1}	415.7 mA h g^{-1}	—	Ship in bottle	Capacity retention of 85.2% after 100 cycles	176

process, a metal hydroxide or colloidal sol undergoes condensation typically catalyzed by an acid or base, or through aging, resulting in the formation of a 3D gel network. In the case of SiO_2, tetraethyl orthosilicate (TEOS) is the primary precursor, and its hydrolysis in the presence of ammonia-water produces an SiO_2 sol network. Additionally, the gel network is formed by the addition of various acids or surfactants. Recently, SiO_2 has been successfully derived from rice husk using the sol–gel method. Generally, an alkali extract of silica is subjected to treatment with nitric acid by keeping pH at 4, which produced the SiO_2 gel.[178] Kennedy *et al.* demonstrated that rice husk represents a naturally abundant source of materials for lithium-ion batteries. This finding suggests that rice husk can also be utilized in applications involving sodium-ion batteries (SIBs), potentially leading to cost reductions.[178] The Nakashima group created a PS–PVP–PEO triblock copolymer consisting of a hydrophobic PS core, an ionizable hydrophilic PVP shell, and a hydrophilic PEO. By adjusting the solution to a low pH (<5) using a mixture of various hydrophilic and hydrophobic substances, acidic condition was generated. This resulted in the formation of micelles in the reaction mixture. The protonated PVP block within these micelles acted as an acidic catalyst site for the hydrolysis of tetramethoxysilane (TMOS), a precursor of silica. Upon stirring the solution containing the micelles, TMOS was added. After allowing the solution to settle for a certain period, a silica network formed. Subsequently, the remaining templates were removed through calcination at a high temperature (>400 °C).[179] Additionally, radicals assisted the polymerization and gel network growth. For instance, Fe_3O_4@SiO_2@PMMA microspheres were prepared *via* the sol–gel method using an aqueous-phase radical polymerization approach. Methyl methacrylate (MMA) underwent radical polymerization in the presence of Fe_3O_4@SiO_2, resulting in the formation of a core–shell structure.[180] Besides, Fe_3O_4/SiO_2,[181] Fe@ZrO_2,[182] C@$MoSe_2$,[183] nitrogen-doped carbon@silica,[184] *etc.* were formed by the sol gel method. Hence, it can be concluded that recent advancements include deriving SiO_2 from rice husk and using triblock copolymers for catalyzing hydrolysis, expanding its applications in battery technologies. Table 6 presents a summary of the electrochemical performances of core shell structures prepared using the sol–gel method (Fig. 6).

3.6.2. Stöber method. The Stöber method is a widely employed sol–gel technique for preparing nanomaterials using

Table 6 Summary of the electrochemical performances of core shell structures prepared using the sol–gel method

Materials	Rate capability	Capacity	Method	Energy density (W h kg^{-1})	Capacity retention	Ref.
$Na_3V_2(PO_4)_3$ (NVP)	94.9 mA h g^{-1} at 5C	—	Sol–gel method	154.5@1.7 V	96.1% after 700 cycles	185
$Na_3V_2(PO_4)_3$	70 mA h g^{-1} at 10C	—	Sol–gel method	—	90% after 400 cycles	186
NaV_3O_8@10% PPy	63 mA h g^{-1} at 3.68C	99 mA h g^{-1} after 60 cycles at 80 mA g^{-1}	Sol–gel method	—	—	187
ZCS@S	250 mA h g^{-1}, 2000 cycles at 1.0 A g^{-1}	570 mA h g^{-1}, 1000 cycles at 0.2 A g^{-1}	Sol–gel method	384		188

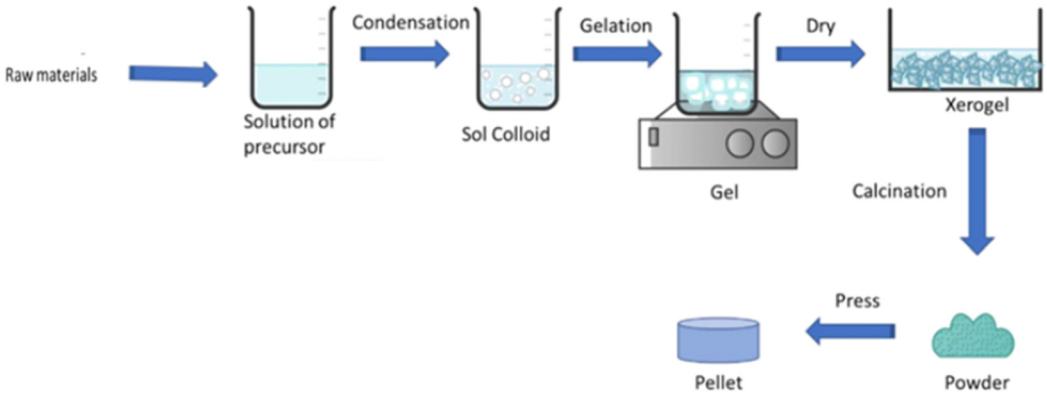

Fig. 6 Schematic view of the sol–gel method.[189] Reprinted with permission from ref. 189. Copyright ©2020, Elsevier Inc.

monodisperse silica nanoparticles. In this method, Si–O–Si bonds are formed through an acid or base-catalyzed condensation reaction, leading to the critical growth of spherical particles. Subsequently, by attaching different electrostatic groups to them, the structure can be tailored in various directions. The Stöber method (as depicted in Fig. 7) involves the synthesis of homogeneous silica spheres from a mixture of tetraethoxysilicate, ethanol, and water in the presence of ammonia. The reaction mixture, after sonication, produces homogeneous colloidal spheres. The Stöber process has been further employed for the preparation of various multicore shell particles through electrostatic interaction with different metal salts or complexes. For the synthesis of SiO_2@Ag core–shell nanosized spheres, tetraethyl orthosilicate was employed as the Si source, while silver nitrate was selected as the Ag source. The Si–OH groups electrostatically interacted with $[Ag(NH_3)_2]^+$ complexes, followed by reduction with PVP, resulting in the formation of SiO_2@Ag core–shell nanosized spheres.[190] A tuneable silica shell thickness with controllable morphology was obtained after varying the temperature and precursors. Different core–shell structures such as ZrO_2@SiO_2 composites,[191] Fe_2O_3@SiO_2@mSiO_2,[192] $NaYF_4$@SiO_2@mSiO_2,[193] and Ag@SiO_2@mSiO_2[194] were synthesized *via* the Stöber method.

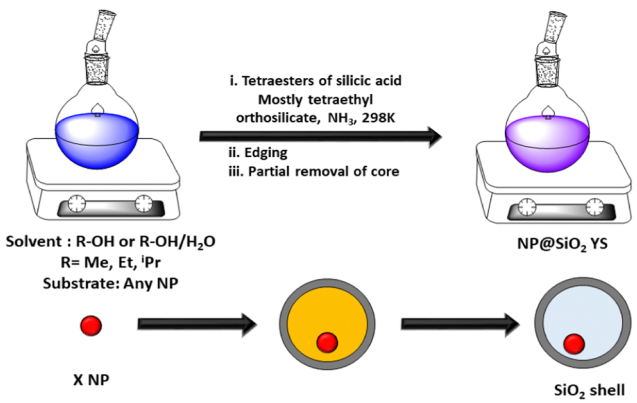

Fig. 7 Schematic design of core–shell/yolk–shell formation *via* the Stöber method.

A mesoporous core–shell structure was obtained through the self-interaction of hydrophobic *n*-octadecyltrimethoxysilane (C_{18}TMS) with a silica template.[195] However, mesopore channels of SiO_2 are also used for tuning the porosity of materials. Importantly, the Stöber method produced a smooth surface with a controllable uniform shell thickness ranging from 2 nm to several μm. Besides, C_{18}TMS, CTAB and other surfactants can provide the porosity on silica. Meanwhile, ethanol/ammonia mixtures can regulate the structures. Increasing the concentration of ammonia, the rational design of core shell structure can be modulated. However, a moderate ammonia concentration is preferable for tunable growth otherwise a too high concentration or low concentration may disrupt the structure or favour Ostwald ripening. The Stöber process produces uniform Fe_3O_4@nSiO_2@mSiO_2[192] microspheres with ordered mesopore channels, which reduce the energy of the core shell. The Xie group showed that the $Na_2Ti_3O_7$@C material synthesized by the Stöber method exhibited a performance of 60 mA h g^{-1} after 1000 cycles at the rate of 50C.[196] Cao and coworkers synthesized a carbon layer with various thickness by the Stöber method, where a 30 nm carbon layer provided a higher reversible capacity.[197] Additionally, the Fang group prepared an $H_2T_2O_5$ material using the Stöber method, where TiO_2 was coated on SiO_2 *via* the hydrolysis method. After treatment with sodium hydroxide, it produced $Na_2T_2O_5$ and *s* tris buffer solution of $Na_2T_2O_5$ produced $H_2T_2O_5$. This material showed exceptional cycle stability after 35 000 cycles at 5 A g^{-1} and high specific capacity of 92.6 mA h g^{-1}.[198] Employing the Stöber method, products with versatile and scalable materials as well as monodisperse, uniform, and tunable products can be obtained. However, in this process, agglomeration and long duration cannot be neglected as disadvantages. In summary, the Stöber method is a sol–gel technique for producing monodisperse silica nanoparticles with a controllable morphology. It enables the synthesis of various core–shell structures, including different MO_x@SiO_2, with uniform shell thickness and ordered mesopore channels. However, although it is versatile and scalable, its challenges include agglomeration and the need for careful control of the reaction conditions and duration. Table 7 displays a summary of the electrochemical

Table 7 Summary of the electrochemical performances of core/yolk shell structures prepared using the Stöber method

Materials	Rate capability	Cyclic capacity	Method	Energy density (Wh kg^{-1})	Capacity retention	Ref.
FeS@C	452 mA h g^{-1} at 5C	545 mA h g^{-1} over 100 cycles at 0.1 A g^{-1}	Stöber method	438	37.8% after 300 cycles	30
Sb@SiO_2@C	149 mA h g^{-1} at 8C	271 mA h g^{-1} over 100 cycles at 0.1 A g^{-1}	Stöber method	142	71.2% after 100 cycles	75
ZnS@S	170 mA h g^{-1} at 5.0 A g^{-1}	570 mA h g^{-1}, 1000 cycles at 0.2 A g^{-1}	Stöber method	384	—	188
$Na_{0.55}Mn_2O_4{\cdot}1.5H_2O$	515.2 mA h g^{-1} at 4.0 A g^{-1}	546.8 mA h g^{-1} at 2000 cycles at 4 A g^{-1}	Stöber method	—	—	199
HCM-Fe_3O_4@ void@N-C	196 mA h g^{-1} at a current density of 1200 mA g^{-1}	522 mA h g^{-1} after 800 cycles at 160 mA g^{-1}	Stöber method	—	—	200
SnS_2@C/CNF	767.6 mA h g^{-1} at 0.2 A g^{-1}	478.7 mA h g^{-1} at 2 A g^{-1} for 1000 cycles	Stöber method		82.4% after 1000 cycle	201

performances of the core shell structures prepared using the Stöber method.

4. Performance based on sodium battery variants

4.1. Sodium-ion batteries (SIBs)

Yolk–shell and core–shell nanostructures offer enhanced performances in SIBs by providing a high surface area, shortened ion diffusion pathways, and improved structural stability during cycling. They can accommodate the volume changes associated with sodium intercalation and deintercalation, thus enhancing the cycling stability and rate capability. Generally, the use of a yolk structure as the anode improves the rate capacity and capacity retention of the material.[202] Similarly, Fe_3N@C[115] and CoSe/C[203] yolk–shell structures are employed as anodes, showing a high rate capability in SIB application. It has been shown that phosphorus, copper, and tin are promising materials for SIB applications. Sometimes metal sulphides also showed a higher contribution to the performance of SIBs such as nickel sulphide due to their ready dissociation and intercalation property.[204] Various strategies and materials have been employed to enhance the performance of sodium-ion batteries (SIBs), aiming to overcome their challenges such as sluggish kinetics, substantial volume changes, and inadequate cycle life associated with specific electrode materials. Nickel sulfide-based materials (NiS, NiS_2, Ni_3S_2, and Ni_3S_4) show promising potential as anode materials for SIBs due to their high theoretical capacity of 873 mA h g^{-1}, as described by the four-electron conversion reaction $NiS_2 + 4Na^+ + 4e- \leftrightarrow Ni + 2Na_2S$.[205,206] However, their sluggish kinetics hamper conversion reactions and lead to significant volume changes during cycling, resulting in a limited capacity and poor cycle life.[205,207] In this case, the addition of carbon has been proven to be effective in enhancing the kinetics and structural stability of the electrode. Yolk–shell NiS_2 nanoparticles embedded in porous carbon fibers (denoted as $NiS_2 \subset$PCF) displayed an excellent electrochemical performance in flexible SIBs. Remarkably, compared to NiS_2 nanoparticles coated on the surface of carbon fibers (NiS_2@PCF), the $NiS_2 \subset$PCF electrode demonstrated a high reversible capacity (679 mA h g^{-1} at 0.1C), good rate performance (42% capacity retention from 0.1 to 10C), and excellent long-term cycling stability (76% retention over 5000 cycles at 5C).[205] Further, the sodiation/desodiation process of the $NiS_2 \subset$PCF electrode was facilitated by the conductive carbon for rapid electron transfer, with its internal porous structure accelerating the penetration of the electrolyte in its channels. Further, the buffer layer expanded to accommodate the strain and volume changes during charge and discharge.[205] Furthermore, the integration of Fe_7Se_8 with carbonaceous materials buffered the stress–strain and enhanced the conductivity. A newly developed Fe_7Se_8-based composite with a porous and intact conductive carbon coating demonstrated a reversible Na-storage capacity of 386 mA h g^{-1} at 100 mA g^{-1}, remarkable rate capability (315 mA h g^{-1} at 5 A g^{-1}), and ultra-long cycle life (no obvious capacity decay over 1000 cycles). Moreover, it exhibited an excellent full-cell performance when paired with a high-voltage $Na_3V_2(PO_4)_2O_2F$ (NVPOF) cathode, suggesting its potential applicability in the Fe_7Se_8@C/N NB//NVPOF full cell.[208] Achieving dendrite-free plating and stripping of sodium, while maintaining high Coulombic efficiencies (CEs) at elevated current densities and capacities, remains a significant challenge. Yolk–shell structures consisting of MnSe/ZnSe heterojunctions embedded within one-dimensional carbon tubes (HCTs) functioned as anode materials for both SIBs and potassium ion batteries (KIBs), enabling efficient insertion and extraction of sodium ions, while establishing a chemical potential gradient. Furthermore, the ZnSe shell enhanced the stability and addressed concerns related to volume expansion.[209] Efforts have been directed towards synergistically incorporating foreign atoms and carbon additives to enhance the performance of battery materials. An example of this is the utilization of nitrogen-doped/carbon-tuned TiO_2 yolk-like materials (NC TiO_2-Y), which demonstrated an exceptional initial coulombic efficiency, remarkable rate capability, and long-term cyclability in SIBs.[210] However, antimony, tin and nickel cobalt integrate the overall performances required in SIB applications,[52,211] and most of the SIB performances are discussed in this context. Hence, a summary of their electrochemical performances is presented in Table 10.

4.2. Sodium metal batteries

In sodium metal batteries, yolk–shell and core–shell architectures are utilized to stabilize the sodium metal anode. These structures can mitigate issues related to dendrite formation

and volume changes during cycling, leading to improved safety, cycle life, and energy density of the batteries.[205,206] The formation of sodium dendrites is linked to the nucleation of sodium metal at the outset and its subsequent growth thereafter.[212] Core–shell C@Sb nanoparticles (NPs) spatially control a physical barrier, which impedes dendrite growth, reduces the risk of short circuits and enhances the battery safety. Furthermore, porous Sb cores offer abundant nucleation sites due to their high surface area and low nucleation barrier, while outer carbon shells prevent agglomeration and dendritic formation.[212] Similarly, C@Ag nanoparticles enable dendrite-free stripping/plating of Na metal together with sodiophilic Ag cores, providing abundant nucleation sites and outer carbon shells ensuring high efficiency during long-term cycling.[213]

4.3. Sodium–sulfur batteries

Yolk–shell and core–shell configurations are also employed in sodium–sulfur batteries to enhance the performance of sulfur cathodes. These structures can confine the polysulfide species, prevent their dissolution, and improve the utilization of active sulfur, thereby increasing the energy density and cycling stability of sodium–sulfur batteries. However, the low conductivity of sulfur (5×10^{-30} S cm^{-1}) and the solubility of lithium sulfide in organic electrolytes result in material loss and create a shuttle effect.[214] However, materials such as MnS_x exhibit a higher affinity to sulfur compared to oxides.[214] Li *et al.* prepared MnS@N–C as the cathode of room-temperature sodium–sulfur (Na–S) batteries, achieving a high initial capacity of 893.9 mA h g^{-1} at 0.1C and demonstrating excellent cycling stability at 0.5C for 300 cycles with a capacity decay of only 0.16% per cycle.[214] Moreover, the incorporation of conducting materials enhances the rate performance and cycle stability of the battery components. Cu nanoparticle-decorated mesoporous carbon spheres showed a promising rate performance and cycle stability.[215] Similarly, the atomic dispersion of cobalt species on hollow carbon nanospheres encapsulated a high content of sulfur. The clustering of cobalt promoted the conductivity of sulfur, enabling a high storage capacity.[215] Fe_2N incorporated into NC yolk shell (YS-Fe_2N@NC) also serves as a sulfur carrier.[30] The hollow microporous structure with a void interior withstands volume strain and accommodated more sulfur particles and soluble polysulfides. Additionally, the nitrogen-doped carbon shell exhibited high conductivity, leading to an outstanding electrochemical performance in sodium–sulfur batteries.[30] Furthermore, porous carbon shells enhanced the conductivity of the active materials, resulting in a high reversible capacity. The nanosized FeS cores provided large electrode/electrolyte contact areas and short diffusion paths for electrons and ions, which improved the sodium reaction rate, mitigated structural degradation, and shortened the Na diffusion paths. The suitable void space buffered the large volume variations of FeS during the sodiation/desodiation processes, maintaining the original nanoparticle morphology of FeS@C and ensuring prolonged cycling stability.[30] Overall, yolk–shell and core–shell nanostructures play a vital role in advancing the performance of sodium-based battery technologies by addressing key challenges related to electrode stability, ion diffusion kinetics, and electrochemical reactions.

5. Performances of core–shell structure in battery application

Core–shell structures have multiple functions such as enhancing the kinetics, effective protection from chemical attack, prevention of pulverisation, SEI layer growth and increasing the conductivity. Hence, core–shell structures can be used as active anodes in sodium ion batteries. It has been investigated that core–shell C@Sb nanoparticles showed extremely higher sodium plating/stripping cycles for 6000 h at a high areal capacity of 4 mA h cm^{-2} with an average Coulombic efficiency of 99.7%.[216] This observation shows that antimony is the best-performing material for sodium metal batteries due to its long-term stable cyclic performance. TiO_2 is another promising material for sodium storage performance. The 600–700 nm yolk-like TiO_2 and 5–10 nm porous carbon structure showed a very high capacity retention of 95.5% after 3000 cycles at 25C.[38]

The specific capacity of sodium ion batteries depends on the controlled thickness, nature, porosity and conductivity of the shell structure. The prevention of the growth of a thick SEI layer is another strategy for enhancing their overall performances. Polydopamine is the best example preventing the growth of a thick SEI layer. The Yu group prepared a phosphorus–CNT@polydopamine (P-CNT) composite, which exhibited excellent cycling stability (470 mA h g^{-1} after 5000 cycles at 5.2 A g^{-1}). Moreover, the coating of polydopamine is the best example as a uniform ion transporter to the interface given that it inhibits the direct contact between the electrolyte and the active material. Furthermore, its large volumetric expansion accommodated a large amount of active materials.[217] Among the transition elements and main group elements, antimony is the best-performing material towards SIB application.

Again, a carbon layer can be used as both a protecting agent and reducing agent of the core material. A resorcinol-formaldehyde layer produced a carbon coating towards different metal oxides and metal sulphides, which acted as a reducing agent and formed a mesoporous conducting carbon coating layer. Yin and co-workers prepared mesoporous hollow core–shell Sb/ZnS@C hybrid heterostructures, where resorcinol-formaldehyde reduced Sb_2S_3 to antimony. The hollow core–shell porous Sb/ZnS@C hybrid exhibited a reversible capacity of 602 mA h g^{-1} and maintained a capacity of about 200 mA h g^{-1} after 600 cycles. In addition, the conducting carbon layer and metallic Sb induced excellent performances.[218]

According to further investigations, it has been noted that iron and vanadium are promising materials for application in SIBs compared to nickel and cobalt. The simple strategy of Ostwald ripening produced FeS@C, which achieved an ultrahigh specific capacity of 632 mA h g^{-1} after 80 cycles at 100 mA g^{-1} and extraordinary cycling stability with a capacity retention of 97.9% after 300 cycles at 1 A g^{-1}. Here, core–shell FeS and interconnected porous graphene greatly enhanced the performance

of SIBs.[219] The Chen group synthesized an NVP@C ($Na_3V_2(PO_4)_3$@C) core–shell structure, which exhibited a reversible capacity of 90.9 mA h g^{-1} at 2C and a specific energy density of about 154.5 W h kg^{-1} at the output voltage of 1.7 V. It also showed an initial capacity of 94.9 mA h g^{-1} at 5C and a noteworthy capacity retention of 96.1% after 700 cycles. The shell carbon originated from ascorbic acid and polyethylene glycol 400. However, this agglomerated core–shell structure contributed less specific capacitance than other materials.[185] Wang *et al.* synthesized a hollow core–shell-type morphology in Zn/Ni–*co*-oxide synthesized from ZIF-67 ($Co(mIm)_2$ (mIm = methylimidazole)). This type of MOF-based hollow shell exhibited a stable capacity of 300 mA h g^{-1} at 50 mA g^{-1} and it showed a stable capacity for 250 cycles.[220]

Morphology is also a vital factor influencing the effective Na-ion and Li ion storage capacity of core–shell structures. Su and co-workers prepared walnut-like porous core–shell TiO_2, where oleylamine modulated the controlled porous morphology, which enabled higher cycle stability for lithium storage.[221] Li *et al.* synthesized a core–shell lychee-like microsphere structure of FeS_2@$FeSe_2$ around a 2–3 μm core structure with a 4 nm pore size, which exhibited a reversible capacity of 350 mA h g^{-1} after 2700 cycles at 1 A g^{-1}. It should be noted that the hydrazine hydrate reduced the precursors and controlled the lychee-like structure.[222] Later, the Zhu group prepared core–shell-like Fe_7S_8@C nano-biscuits, delivering 530.8 mA h g^{-1} after 1000 cycles at a high current density of 5 A g^{-1}. In addition, the thioacetamide solution successfully fabricated the desired morphology and provided the surface area of 39.22 m^2 g^{-1} and micropore size of 0.56 nm, where the short and easy diffusion pathways accommodated the electrolyte ions.[223] Between the nanorod and nanowire morphology, the nanorod morphology shows slightly greater advantage. The Kang group prepared a CoP@PPy NW/carbon paper 1D core–shell structure delivering a high areal capacity of 0.521 mA h cm^{-2} at 0.15 mA cm^{-2} after 100 cycles. The 1D core–shell-type nanowire on carbon fibre well-controlled the volume expansion during charge/discharge.[224] Xu *et al.* prepared $BiSbS_3$@N-doped carbon core–shell nano-rods, resulting in a high sodium storage capacity of 771.5 mA h g^{-1} in the 2nd cycle and excellent rate capacity at 1000 mA g^{-1}.[225]

Later, we investigated the contribution of morphology such as nanofibers and nanoribbon structures. Lu and co-workers prepared Ge@graphene@TiO_2 core–shell nanofibers *via* atomic layer deposition (ALD), which exhibited the reversible capacity of 182 mA h g^{-1} at 100 mA g^{-1} (250th cycle). The ultrathin thickness of the TiO_2 coating protected the Ge@G (core–shell Ge@graphene@TiO_2) from the electrolyte, where the SEI layer of Ge was less predominant than the new SEI layer by TiO_2. The well-defined nanofiber architecture maintained its architecture after five cycles at the current density of 100 mA g^{-1}.[226] The Srinivasan group prepared a nano-ribbon-type core–shell structure (MWCNT@graphene oxide nanoribbon), which decreased the restacking ability of graphene and provided a capacity of 317 mA h g^{-1} at a current density of 50 mA g^{-1}. The MWCNT shell material enhanced the rate capability owing to its high electronic conductivity and abundant functional groups on the graphene layer increasing the adsorption of Na^+ on the surface.[227]

Besides, 2D- and 1D-like structures, polyhedron-like facet structures have also been investigated for their application in SIBs. Yin *et al.* prepared a ZnS–Sb_2S_3@C core-double-shell polyhedron, which exhibited a high reversible capacity of 630 mA h g^{-1} at 100 mA g^{-1} after 100 cycles.[228] However, its double shell polyhedron-like structure helped to extend its reversible capacity compared to its cyclic stability, as discussed in the earlier reports. Further, rechargeable all-solid-state sodium batteries are one of the most promising high-safety energy storage devices compared to all sodium-ion batteries. Yao *et al.* prepared a rod-like core–shell structured $Fe_{1-x}S$@$Na_{2.9}PS_{3.95}Se_{0.05}$ electrode, which possessed an extremely high energy density of 910.6 W h kg^{-1}.[229] Moreover, acetonitrile controlled the higher conducting cubic morphology with a particle size of 500 nm. This a core–shell structure reduced the side reaction between $Fe_{1-x}S$ and $Na_{2.9}PS_{3.95}Se_{0.05}$.

6. Performances of yolk shell structure in battery application

Yolk–shell structures have specially attracted interest for application in sodium batteries given that they prevent the pulverization process during charging and discharging.[230] Similarly, in the case of core shell structures, it has been noted that tin, antimony and iron are promising materials for enhanced sodium storage capacity. Kim and co-workers prepared Fe_3O_4@N-doped carbon (NC) yolk–shell from Fe_2O_3 nanoparticles and dopamine hydrochloride followed by etching in an acidic medium and calcination in an argon atmosphere at 500 °C for 5 h. The NC provided numerous active sites and effective electronic conductivity. The distinctive voids in the Fe_3O_4@NC yolk- and yolk–shell structure exhibited a high reversible capacity of 594 mA h g^{-1} over 100 cycles at 100 mA g^{-1}.[231] The yolk–shell iron sulfide–carbon nanospheres exhibiting porous carbon shells (~30 nm) and void space (~20 nm) originating from the etching of the silica particles enabled an enhanced sodium storage capacity. In addition, this nanosized iron sulfide–carbon exhibited a capacity of 545 mA h g^{-1} over 100 cycles at 0.2C (100 mA g^{-1}).[96] However, decreasing the carbon shell thickness to 10 nm in Sn_3P_4@C yolk–shell materials resulted in a higher cycling performance (516 and 368 mA h g^{-1} after 500 cycles at 1.0 and 2.0 A g^{-1}, respectively). Furthermore, the carbon nanocubes could buffer the volume expansion better than the fibre structure.[128]

When the yolk shell is combined with carbon spheres, the cyclic stability increases. Kang *et al.* synthesized wrinkled nanosheets of yolk–shell-structured $MoSe_2$ microspheres using hydrogen selenide vapour at 300 °C, exhibiting a sodium storage capacity of 433 mA h g^{-1} after 50 cycles at a current density of 0.2 A g^{-1}. Here, the wrinkled nanosheets of yolk–shell-structured $MoSe_2$ enabled the sodium storage capacity.[232] Further, when it was modified with porous carbon, its cyclic

stability increased. Chen and co-workers prepared yolk–shell NiS_2 nanoparticles on porous carbon fibres from $Ni(NO_3)_2$ *via* hydrophilic treatment on the channels of porous carbon fibres, exhibiting a high reversible capacity of 534 mA h g^{-1} after 300 cycles at 0.1C with 85% capacity retention. Additionally, the material exhibited a high-rate capacity of 245 mA h g^{-1} at a high rate of 10C. This excellent performance is attributed to its highly porous structure obtained from a longer duration of heating treatment, resulting in a surface area of 949 m^2 g^{-1} and the presence of both micropores (<2 nm) and mesopores (5–15 nm).[233]

As another factor, the morphology of materials is another vital parameter enabling the sodium storage capacity. The modification of 1D-like structures with transition elements contributes an excellent performance towards SIB application. A necklace-like structure composed of Fe_3N@C yolk–shell, obtained from polyacrylonitrile through the electrospinning method, exhibited good cycling stability and a capacity of 248 mA h g^{-1} at 2 A g^{-1}.[115] Its excellent performance emphasized that Fe_3N or PAN fiber enlarged the performance than the previously discussed Fe_3O_4 or iron sulphide. Moreover, voids can be intentionally designed within the electrode structure to improve the ion diffusion pathways and enhance the accessibility of the active material to the electrolyte ions. Voids or empty spaces within a battery reduce the overall mass of the battery without sacrificing the active material. Given that the energy density is typically measured in terms of energy per unit mass, by reducing the mass, a high energy density is obtained.

Although it is difficult to compare the performances of different compounds with different morphologies, overall microspheres show a higher performance compared to wires. Likewise, the yolk–shell SnO_2@void@C nanowires synthesised using polyethylene glycol-400, followed by etching of the SiO_2 layer showed a capacity of 401 mA h g^{-1} at a current density of 50 mA g^{-1}.[126] Further, polyhedron compounds have attracted considerable interest in SIB application. The Zhang group prepared Sb@C yolk–shell microspheres, which revealed a reversible capacity of 400 mA h g^{-1} after 300 cycles with 1 A g^{-1}.[234]

A yolk–shell mesoporous octahedron-like structure delivered a capacity of 597.2 and 361.9 mA h g^{-1} at 0.2 and 16 A g^{-1}, respectively. Moreover, octahedron yolk–shell structures were formed by the Kirkendall effects between Se and Co on ZIF-67. Their pore size was found to be in the range of 2–10 nm, showing an excellent rate capability.[203] Besides, yolk–shell nano-boxes have attracted considerable attention due to their sodium storage capacity.[235] The Zhou group prepared yolk–shell Fe_7S_8@C nano-boxes and Fe_3O_4@C nano-cubes. The yolk–shell Fe_7S_8@C nano-boxes exhibited a higher cycle stability and higher coulombic efficiency than the cubic structure.[236] Again, the double shell cube-like structure showed very high cycle stability. Recently, yolk–double-shell cube-like SnS@N–S co-doped carbon exhibited a capacity retention of 83.5% at 1 A g^{-1} after 1500 cycles.[237] Mai and co-workers prepared a mesoporous CoS yolk with alveolus-like carbon shell, which exhibited the outstanding cyclic capacity of 532 mA h g^{-1} after 100 cycles at 0.2 A g^{-1}.[238] The alveolus-like carbon shell appeared from the resorcinol formaldehyde structure. However, the polydopamine coating box-like hollow yolk shell contributed a higher performance than the resorcinol formaldehyde coating. Among the transition-metal yolk–shell hollow spheres, $NiCo_2O_4$ yolk–shell,[14] Ni_2P@C yolk–shell nanocomposite,[239] GF/FeS_2@C,[240] and yolk–shell $CoMoO_4$ nanospheres[241] have been found to be efficient sodium storage materials.

7. Comparative overview

Aerosol synthesis[242] is a cost-effective, attractive, and scalable method for the preparation of materials. There are several aerosol spray methods such as spray-drying,[243] aerosol-spray-freezing,[244] spray pyrolysis[245] and ultrasonic spray pyrolysis. However, all these techniques depend on the temperature, concentration and other parameters. Among these techniques, aerosol-spray pyrolysis has attracted considerable attention due to its industrial-scale production with a short time and high purity grade. Hence, this is a promising and economical technique for battery application.[242] In the case of ultrasonic spray pyrolysis, an ultrasonic nebulizer coverts a homogeneous salt mixture into droplets at the hot zone of a tubular furnace, which upon cooling form solid particles. The obtained dried particles without calcination process form spherical porous particles.[246] Zhang *et al.* described in detail the aerosol method for battery application.[242,247] Hence, we focus on the materials generated through the aerosol pyrolysis method that contribute a higher performance. Among the elements, it has been shown that tin-based materials have comparatively higher performances and cycle stability compared to other transition-metal-based compounds due to the higher tendency of tin to form alloys with sodium. Recent research showed that an Sn@C nanocomposite with 46 wt% Sn delivered an initial reversible capacity of ≈493.6 mA h g^{-1} at the current density of 200 mA g^{-1} and a stable capacity of ≈ 415 mA h g^{-1} after 500 cycles at 1000 mA g^{-1},[248] whereas other transition elements such as $CoSe_x$–rGO composite displayed a capacity of 420 mA h g^{-1} at a current density of 0.3 A g^{-1}.[249] Recently, Kang and co-workers described in detail the metal chalcogenides synthesized *via* the spray pyrolysis method employed as electrode materials. Among these materials, FeS prepared through the spray pyrolysis method showed the highest discharge capacity and cycle stability.[250] The role of the diameter of spherical materials has also been considered for SIB applications. Wang and co-workers synthesized 200–300 nm NiS_2 nanoparticles, which showed the capacity retention of 77% at 0.1C for 200 cycles.[206] The Sb@S,N-doped-3D interconnected nanoporous carbon electrode with a cavity of 200 nm exhibited ~93% of its initial discharge capacity after 500 cycles at 100 mA g^{-1}.[251] Further, a reduction in its diameter to less than 10 nm showed an enhanced capacity retention of 81% after 2000 cycles at 1 A g^{-1}.[252]

Several reports exhibited that the wrapping of materials with carbon increases their electrochemical performances. The thickness of the carbon coating depends on the reaction time, concentration of the reactants and temperature. A moderate

thickness can lead to a significant enhancement in performances. In a few studies, it was observed that the outer conducting cell remarkably enhanced the performance. Feng *et al.* applied 200 mL pyrrole on 200 mg $CuCo_2S_4$ spheres, forming a 30 nm outer-layer coating, which exhibited remarkable cycle stability at 2 A g^{-1}.[253] It was observed that the addition of 5-times urea to ferric acetylacetonate formed a 10–15 nm outer carbon coating, delivering 500 cycles at 2 A g^{-1}, which is comparatively less than that of the 30 nm polypyrrole coating.[254] Further, keeping a 13–20 nm carbon layer on Sn_2S_3 spheres slightly reduced the cycle stability compared to the polypyrrole coating.[255]

The performances of yolk/core shell structures depend on the yolk and core as well as on the shell structure. Yolk–shell structures cannot only reduce the transmission resistance of lithium and sodium ions but also promote the diffusion dynamics of ions/electrons by shortening the transmission path. Importantly, the unique architecture provides a buffer space for volume changes caused by the insertion/extraction of Li^+/Na^+. Thus, the structural stability of the electrode material is guaranteed, confirming its good Li/Na-storage performance between the yolk–shell and core–shell structure.[256] Also, lithiation depends on the void space in the yolk and shell structure. Given that the sodium ion is larger than the lithium ion, a higher void space is required in SIBs compared to the smaller void space for Li-systems.[257] The commercialization of sodium batteries is mainly associated with the sodium ion battery. Hence, here, we discuss the stability and corresponding parameters in the sodium ion battery. It is assumed that the application of yolk–shell and core–shell structures in sodium ion batteries will be a major attraction in the near future.

Core–shell structures offer large electrode/electrolyte contact areas and increase the sodium diffusion rate by controlling the diffusion path.[258] Further, the void space in yolk shell structures can suitably control the sodiation/desodiation processes by buffering the core in the large void space, which facilitate the cycling stability and enhance the energy density.[258] A literature review also suggested that yolk shell structures have a higher surface area compared to core shell structures. Moreover, sodium sulphur batteries have recently become a popular area of research.

In sodium sulphur batteries, conversion occurs through the insertion of sodium into the core structure of Na_2S or Na_xS with multiple redox states. Thus, prolonged cycle stability can be achieved in core–shell or yolk–shell structures.[259] The special contribution of yolk shell and core–shell structures is the electrolyte interface (SEI) on the electrode, which further increases the overall efficiency.[260] An SEI layer is a crucial factor in the overall performances of batteries. A stable and well-formed SEI layer is essential for the battery performance, given that it improves the cycling stability, prevents capacity loss, and enhances safety by inhibiting further electrolyte decomposition and dendrite formation. The additional shell material for the yolk or core acts as a protective layer, but still there is a possibility of the formation of electrode and electrolyte interactions, forming an SEI layer. In this case, porous shell materials can form a uniform thin SEI layer, while a very thick SEI layer may be responsible for irreversible capacity loss.[260] Further, the excessive growth of an SEI layer leads to increased internal resistance, capacity fading, and reduced battery performance over time.

It is difficult to draw a conclusion on efficacy of different yolk- and core–shell structures given that there are several factors to consider such as different metal centres, shell thickness, conductivity, and diameter of hollow structure. However, an overview of this topic can predict their net result and best performance for industrialization. It is well known that chalcogenide structures are interesting to achieve an enhanced sodium storage capacity due to their intercalation property.[261] Among the heterostructures of SNS@MoS_2, the yolk–shell structure showed a higher performance and comparatively low shifting of the SEI film compared to its dense structure.[262,263] In addition, the dense structure showed lower charge transfer resistance compared to the yolk–shell structure, which also resulted in better performances.[263]

The EV market is dominated by Li-batteries. A new lithium titanium oxide anode showed direct contact with the electrolyte and a very thin SEI film of Li_2O appeared, which would not impede the diffusion of lithium ion. Due to the absence of a very thick SEI film, the unchanged resistance as well as transport ability and stable structure over the electrolyte enhanced the prolonged cycle stabilty.[264] Also, a few other factors such as safety, recycling ability, cost effectiveness, cobalt-free electrode, material supplier, and stoichiometry ratio of metal to Na-ions should be optimized. Henceforth, specifically designed yolk- and core–shell structures associated with these factors can substantially realize the future capacity goal.

8. Machine learning on sodium battery

Machine learning has a huge scope for the enhancement of battery technology and robust performance of sodium batteries. Machine learning algorithms are utilized for the improvement in overall battery health, *i.e.* cyclability, charging time and discharging time.[265,266] It also improves the battery management system and the design of the electrolyte, cathode, and anode materials through the use of several existing experimental details. Hence, in a very rapid time, machine learning can predict the overall battery health. Furthermore, machine learning reduces the computational time and needs less data storage facilities given that the calculations are performed within a very short time. Again, it reduces the optimization steps of material preparation, and hence the material cost and overall experimental steps can be reduced. Specifically, it can be concluded that machine learning can predict materials design for fast charging capacity and highly durable battery technologies, which eventually benefit the overall production process. However, to achieve promising experimental conditions as well as the material details, a large dataset is needed, which is first pre-processed and cleaned through algorithms. This processed data is trained through a machine learning

model and tested by different datasets.[267] The model is chosen by matching the pattern of the dataset. Hence, after training of the datasets, the model predicts the accuracy score of the test data. The accuracy score could be evaluated through the root mean square value. The model is chosen by taking 90% accuracy of data prediction.[268] The cycle stability of a battery continuously fed through time results in an increase in impedance and decrease in capacity. Hence, the machine learning model will develop after considering the cycle stability based on several commercial battery data. For dataset preparation, a large scale of commercial datasets is needed. However, sodium batteries are not as commercialized as lithium ion batteries. Hence, based on lithium battery datasets, the cycle stability and other parameters can be optimized. Zhang *et al.*[269] prepared an advance dataset from the MIT database, where 124 commercial data were recorded within normal capacity of 1.1 A h. After collecting the data, namely feature extraction and feature selection were employed. A total of 42 features was extracted on battery degradation data from the first 100 cycles. Next, the feature dimensions were reduced by employing the filter, wrapper, embedded, and principal component analysis (PCA) methods. After, feature cleaning, different machine learning models such as elastic net, GPR, SVM, random forest (RF), GBRT, and NN were employed for the determination of the battery lifetime. They identified the SVM model as the best model for the accurate prediction of the battery lifetime.[269] Recently, Yildirim *et al.* described the discharge capacity with a variation in the electrode preparation method, cathode material, and anode material. They arranged the data with the variation in different parameters from 355 experimental papers. Gradient boosting, support vector machines, random forest, (for regression), and decision tree (for classification) methods were used for the data analysis. They analyzed that the anode material and preparation methods are highly effective in determining the cycle stability.[270] Chen *et al.*[271] described over 160 NASICON materials through random forest (RF) and neural network (NN) models. They implied suitable NASICON electrolyte design for SIBs.[272] Yildirim and co-workers also collected 1227 data points from 335 published papers and applied random forest (for discharge capacity prediction) and decision tree (classification).[271] Chao *et al.* described different carbon-based materials as anodes for sodium batteries. They correlated the structure and synthesis of different carbon materials with their discharge capacity. The result shows that hard carbon with a high I_D/I_G value is the advanced adaptor for SIBs.[273] However, manganese can be a promising material for improving the performance of SIBs, as it can achieve a high energy density of 133.1 W h kg^{-1}, which can be further applicable for power grid applications.[274] Zhang *et al.* prepared the manganese-based material P2-$Na_{0.67}Ni_{0.33}Mn_{0.67}O_2$, which showed record operating voltage windows beyond 3.5 V in a full cell and may be helpful for designing yolk/core shell-like structures with significant results.[275] Recently, Dong *et al.* described a nickel–manganese material to enhance the discharge capacity of sodium batteries.[276] They corelated different factors such as the amount of nickel and various dopants in the dataset. Their results showed better cycle stability depending on the nickel content. Hence, based on the overall literature analysis, it can be concluded that the dataset parameters are constructed using the FWHM value from XRD, Raman I_D/I_G value, and crystal system from XRD. The discharge capacity is summarised employing a particular cycle stability. Therefore, it can assumed that the discharge capacity with various parameters can be correlated by the correlation method and the prediction of discharge capacity can be done by regression analysis. Furthermore, the cycle stability could be determined by classification tests.

9. Advantages of yolk–shell and core–shell structures in sodium batteries

Yolk–shell structure

Cycling stability. The hollow core provides space for the volume expansion of the active material, reducing mechanical stress and preventing pulverization. The hollow core structure increases the cycling stability as well as the reversible capacitance of electrodes. Besides, it enhances the electrode kinetics and structural stability of the material.[43a]

Specific capacity. The yolk–shell structure consists of a hollow core (the yolk), which is surrounded by a shell. This porous yolk shell structure allows the accommodation of volume changes during cycling, which extends the specific capacity of electrode materials. The large void space also protects the SEI layer from cracking. The porous shell and void space help to grow a thin SEI layer, which maintains the cyclic stability. However, dual or triple materials increase the mechanical stability and a high loading increases the rate, duration and storage performance.[147]

High rate capability. The yolk–shell structure improves the ion diffusion rate and electron transport pathways, leading to a high rate capability.[147]

Core–shell structure

Stabilization of active material. In core–shell structures, the active core material is encapsulated within a porous shell material. This encapsulation provides stability to the active material, preventing undesirable side reactions with the electrolyte and enhancing the cyclic stability.[199]

Prevention of agglomeration. Core–shell structures can prevent the formation of dendrites on the sodium metal, ensuring a higher battery lifetime, capacity retention and cycling stability. The porous shell carbon material also increases the conductivity of the material and increases the exposure of electrodes and electrolyte without damaging the core materials.[200]

Ion diffusion. The porous shell material in core–shell structures can be engineered to control the diffusion of ions, which increases the high rate performance.

10. Summary and conclusion

Researchers have devoted their efforts to developing sodium-ion batteries with the aim of achieving a higher capacity, while

maintaining affordability compared to lithium batteries. They are anticipated to find widespread use, ranging from wearable electronics, laptops, and mobile phones to electric vehicles, due to the abundance of sodium resources compared to lithium. However, a recent article in Nature Communications suggests that alkaline medium is superior to aqueous or neutral medium for sodium batteries.[277] Companies such as Tiamat, Faradion, and Novasis are further assembling Na ion batteries in 18 650 form factor (18 mm diameter, 65 mm length and O indicates cylindrical cell) or as pouch cells.[2] For comparison, 18 650-size commercial Na-ion batteries with hard carbon as the anode showed a specific energy of 150 W h kg^{-1}, which is close to that of $LiFePO_4$ in 18 650-size commercial Li-ion batteries. This energy density can be applied in small EV, solar cells, power grid, *etc.*[278]

In summary, novel single, multi-core–shell and yolk–shell structures have been designed with high facile surface area and conductive network towards sodium batteries. This perspective summarized the reports on core–shell and yolk–shell structures. The yolk shell and core shell structures showed energy storage and volumetric expansion during their charge discharge step. The capacity performance in sodium batteries also depends on the cell construction, type of electrolyte, cell binder, and temperature. Further investigation showed that the multi-shell cavity or porous channels of MOF-based structures increase the rate capability and capacity retention.[279–281]

However, the higher performances of yolk–shell structures are attributed to their adequate internal space, facilitating large volume expansion, shortened diffusion distance and more active sites of Na^+.[282] In this perspective, core–shell and yolk–shell structures both showed similar sodium storage capacity, but the cycle stability and rate capacity are slightly higher in the case of the yolk–shell structure. The sodium storage capacity further depends on the carbon architecture such as RF,

Table 8 Capacity performances of core shell structures in sodium ion batteries

Catalyst	Current density (mA g^{-1})	Capacity (mA h g^{-1})	Cycle stability	Energy density	Capacity retention	Ref.
P-doped NiS_2/C	500	766.8	400	—		283
FeS_2@C	100	616	100	—		284
Bi@Void@C	20 000	198	10 000	—	96% after 10 cycles	50
FeS@mesoporous carbon	200	596	100	—		285
Bi_2S_3/C	0.2C	282.4	300	—		25
Sb@NS-3DPCMSs	20 000	331	10 000	—		286
$NiCoSe_2$/CNT	3000	366	10 000	—		26
$NiCo_2O_4$	100	314	100	—	—	14
N-doped carbon coated FeS_2 nanocages	5000	375	1000		92%	287
TiO_2 microspheres	50	230.7	200		91.7% after 1000 cycles at 1 A g^{-1}	288
Sb@C yolk–shell microspheres	5000	633	200		99% over 200 cycles	289
Sb@C	1000	400	300	—	—	234
($Fe_{1-x}S$)@N-doped carbon (FS@NC)	100	594	100	—	—	231
Fe_3N@C Yolk–Shell Particles	2000	248	300			115
SnO_2 yolks and graphene shells	1000	248.2	1000	—	86.9%	202
SnS_2@C	100	690	100	—	87% after 150 cycles at 1 A g^{-1}	290
Sb@C	10C	315	—	130 W h kg^{-1}	92% over 200 cycles at 1C rate	291
Sn_4P_3@C	1 A g^{-1}	516 mA h g^{-1}	500		55.3%	128
Sb@C	1000	280	200	—	—	114
CoSe/C	16 000	361.9	—	—	—	203
TiO_2@C	40C	210	2000		85%	292

Table 9 Capacity performances of core shell structures in sodium ion batteries

Catalyst	Capacity (mA h g^{-1})	Current density (A g^{-1})	Cycle stability	Energy density	Capacity retention	Ref.
$NaTi_2(PO_4)_3$@polyaniline	104.1	10C	200	—	96.9% after 200 cycles	293
Sn@C	>500 mA h g^{-1}	0.2C	300	—	80.1% at 0.2C after 300 cycles	294
P–CNT@PD composite	730	2.6	2000	—	—	217
Sb_2S_3	604	2 A g^{-1}	—	—	—	295
Sb/ZnS@C	613	0.1	100	—	—	218
ZnS-Sb_2S_3@C	630	0.1	120	—	—	228
rGO/Sb_2S_3	306	0.1	60	—	—	296
$Na_5V_{12}O_{32}$@PPy	202	0.1	100	—	97% after 100 cycles	297
CNF@NPC	240	0.1	100	—	—	298
SnO_2@PANI	213.5	0.3	400	—	—	299
Ge@G@TiO_2	182	0.1	250	—	—	226
Ni_2P@C/GA	253.6	0.1	100	—	—	300
Nb_2O_5@C NPs to rGO	285	0.025	—	76 W h kg^{-1}	—	301
$Fe_{1-x}S$@SC	454.3	1.0	500	—	—	302
Sb@$Co(OH)_2$	555.9	0.5	180	—	—	303
Co_9S_8@C/3DNCF	400.4	1	1400	—	—	304

Table 10 Summary of electrochemical data for yolk–shell/core–shell structures in sodium batteries

Sample	Cyclic capacity	Coulombic efficiency	Reversible capacity	Rate capability	Capacity retention	Energy density	Full cell	Ref.
Sodium ion battery								
Yolk–shell P-doped NiS_2/C	—	72.9%	1113.5 mA h g^{-1} at 0.1 A g^{-1} after 20 cycles	766.8 mA h g^{-1} at 0.5 A g^{-1} after 400 cycles	—	—	—	283
Nickel–cobalt selenide carbon yolk shell	344 mA h g^{-1} over 200 cycles at 0.5 A g^{-1}			237 mA h g^{-1} at 5 A g^{-1}.	After 2nd cycle @98%	—	—	305
Yolk–Shell Sb@Ti–O–P	760 mA h g^{-1} after 200 cycles at 500 mA g^{-1}	94%	360 mA h g^{-1} at 10 A g^{-1}	—	—	—	392 mA h g^{-1} anode after 150 cycles at 1 A g^{-1} at high output voltage (~2.7 V)	306
$FeSe_2$@NDC-NBs	403.3 mA h g^{-1} over 2000 loops at 5.0 A g^{-1}	99% after 2nd cycle (full cell)	106.4 mA h g^{-1} at 1C after 100 loops	374.9 mA h g^{-1} at 10.0 A g^{-1}	—	—	Reversible discharge capacity of 312.5 mA h g^{-1} anode after 100 cycles at 2.1 V	307
ZnSe-NC@$CoSe_2$-NC core shell	—	56.9@150 cycles	308.5 mA g^{-1} after 150 cycles at a current density of 0.1 A g^{-1}	—	—	—	—	308
$CoSe_2$@$NiCoSe_4$-NC yolk shell	Specific capacity of 341.3 mA h g^{-1} at a current density of 5 A g^{-1}	—	—	—	94.8% after 400 cycles at 1 A g^{-1}	—	—	309
Sn/Cu_6Sn_5@N–C yolk shell	—	ICE = 84.9%	440.1 mA h g^{-1} after 1000 cycles at 1 A g^{-1}	486.6 mA h g^{-1}@10C	90.8% @10C	—	—	52
FeS/C yolk shell	300.4 mA h g^{-1} after 10 000 cycles at 10 A g^{-1}		664.9 mA h g^{-1} at 0.1 A g^{-1}		81.1% after 10 000 cycles (half-cell)/71.9% after 1000 cycles at 2 A g^{-1}	181.9 W h kg^{-1} at 0.05 A g^{-1} (full cell)		27
ZnCoSe@ NDC yolk shell	344.5 mA h g^{-1} at 5.0 A g^{-1} over 2000 cycles	99% after 200 cycles		319.2 mA h g^{-1} at 10.0 A g^{-1}	96.3% of its initial capacity at 0.5 A g^{-1} after 200 loops (full cell)		Reversible discharge/charge capacity of 340.6/335.9 mA h g^{-1} after 200 cycles @2.1 V	310
Fe_{1-x}/SWNT@C yolk shell	710 mA h g^{-1} after 100 cycles at 0.1 A g^{-1}	99 – 100%		317 mA h g^{-1} at 20 A g^{-1}				311
YDSC-SnS@NSC yolk shell	—	—	—	257 mA h g^{-1} at 8 A g^{-1}	83.5%@1 A g^{-1}	—	—	312
NiS_2/CuS yolk shell	283.4 mA h g^{-1} even after 4200 cycles at 20.0 $^{-1}$.	ICE of 94.0%	—	—	—	—	—	313
NiS_2 ⊂ PCF yolk shell	—	—	679 mA h g^{-1} at 0.1C	245 mA h g^{-1} at 10C	76% @5000 cycles at 5C	—	—	233
Yolk–Shell MnSe/ZnSe	408.5 mA h g^{-1} even after 1000 cycles at 0.1 A g^{-1}	—	—	475 mA hg^{-1} at 0.1 A g^{-1}	72% after 1000 cycles at 100 mA g^{-1}			209
Fe_7Se_8@C/N yolk shell	No decay in 1000 cycles			316.0 mA h g^{-1} at 5 A g^{-1}	98% after 100 cycles (full cell)	216 W h kg^{-1}		208
Sodium metal battery								
Core–Shell_C@SbNP	6000 h at a high areal capacity of 4 mA h cm^{-2} with an average CE 99.7%	99.7%	—	—		—	—	212
C@Ag yolk shell	—	99.7% at 1 mA h cm^{-2} for more than 2000 cycles			80.7@after 320 cycles (full cell)		71 mA h g^{-1} after 320 cycles	314
Sodium sulphide battery								
S/YS–Fe_2N@NC yolk shell	467 mA h g^{-1} after 350 cycles			Specific capacity of 1123 mA h g^{-1} at the rate of 1C				215
FeS@C yolk shell	545 mA h g^{-1} over 100 cycles at 0.2C (100 mA g^{-1})				Capacity retention of 67.6% after 300 cycles	438 W h kg^{-1}		30

polydopamine, and PEG. Alternatively, multichannel hollow porous core–shell structures may be beneficial for SIB applications. In hollow core–shell structures, sodiation and desodiation are much faster compared to their core–shell counterparts. The creation of voids between the core and outer shell prevents excessive expansion during the alloying or dealloying process. Further, the mesoporous size and void size also regulate the capacity performances. With a successive decrease in pore size, the reversible capacity increases. The best capacity is achieved with a 3–4 nm mesoporous channel. Further, with a decrease in the size of the core particle to ~2.4 nm, the reversible capacity can be controlled was also noted that a conducting coating or metallic core and yolk-like structure show a lower resistance. Finally, regulating other factors such as low contact angle, maximum exposure of the electrolyte, and small size of the core particles will help attain a higher rate capability and stability. Tables 8–10 present a summary of all types performances in sodium batteries.

Author contributions

Anurupa Maiti: writing – original draft, Visualization, review and editing. Rasmita Biswal: review. Soumalya Debnath: Drawing. Anup Bhunia: review and editing.

Conflicts of interest

The authors declare no conflicts of interest.

References

1 Y. Wang, D. Zhou, V. Palomares, D. Shanmukaraj, B. Sun, X. Tang, C. Wang, M. Armand, T. Rojo and G. Wang, *Energy Environ. Sci.*, 2020, **13**, 3848–3879.
2 J.-M. Tarascon, *Joule*, 2020, **4**, 1616–1620.
3 J. Lihua Liu, R. Dong and M. Danilovic, *Electrification of the transportation system in China: exploring battery technology for electrical vehicles in China 1.0, Sweden-China Bridge: Collaborative Academic Platform for the Electrification*, 2021, Top 10 sodium ion battery manufacturers in China, L. Li, **https://www.takomabattery.com/top-10-sodium-ion-battery-manufacturers-in-china/#CATL**.
4 H. Yadegari, Q. Sun and X. Sun, *Adv. Mater.*, 2016, **28**, 7065–7093.
5 C. Delmas, *Adv. Energ. Mater.*, 2018, **8**, 1703137.
6 S. Chen, C. Wu, L. Shen, C. Zhu, Y. Huang, K. Xi, J. Maier and Y. Yu, *Adv. Mater.*, 2017, **29**, 1700431.
7 C. B. Tabelin, J. Dallas, S. Casanova, T. Pelech, G. Bournival, S. Saydam and I. Canbulat, *Miner. Eng.*, 2021, **163**, 106743.
8 H. S. Hirsh, Y. Li, D. H. Tan, M. Zhang, E. Zhao and Y. S. Meng, *Adv. Energy Mater.*, 2020, **10**, 2001274.
9 Y. Wang, D. Zhou, V. Palomares, D. Shanmukaraj, B. Sun, X. Tang, C. Wang, M. Armand, T. Rojo and G. Wang, *Energy Environ. Sci.*, 2020, **13**, 3848–3879.
10 J. F. Peters, M. Baumann and M. Weil, In *The importance of recyclability for the environmental performance of battery systems, Cascade Use in Technologies 2018: Internationale Konferenz zur Kaskadennutzung und Kreislaufwirtschaft–Oldenburg 2018*, Springer, 2019, pp. 104–110.
11 Z.-X. Huang, X.-L. Zhang, X.-X. Zhao, Y.-Y. Zhao, V. Aravindan, Y.-H. Liu, H. Geng and X.-L. Wu, *Inorg. Chem. Front.*, 2023, **10**, 37–48.
12 R. Chen, D. Bresser, M. Saraf, P. Gerlach, A. Balducci, S. Kunz, D. Schröder, S. Passerini and J. Chen, *ChemSusChem*, 2020, **13**, 2205–2219.
13 N. Yabuuchi, K. Kubota, M. Dahbi and S. Komaba, *Chem. Rev.*, 2014, **114**, 11636–11682.
14 Y. Zhang, X. Xiao, W. Zhang, Y. Liu, J. Zhong, M. Chen, X. Fan and L. Chen, *J. Alloys Compd.*, 2019, **800**, 125–133.
15 K. Chayambuka, G. Mulder, D. L. Danilov and P. H. Notten, *Adv. Energy Mater.*, 2018, **8**, 1800079.
16 W.-J. Zhang, *J. Power Sources*, 2011, **196**, 13–24.
17 B. Scrosati, J. Hassoun and Y.-K. Sun, *Energy Environ. Sci.*, 2011, **4**, 3287–3295.
18 Y. You and A. Manthiram, *Adv. Energy Mater.*, 2018, **8**, 1701785.
19 Y. X. Wang, B. Zhang, W. Lai, Y. Xu, S. L. Chou, H. K. Liu and S. X. Dou, *Adv. Energy Mater.*, 2017, **7**, 1602829.
20 L. Xiao, F. Ji, J. Zhang, X. Chen and Y. Fang, *Small*, 2023, **19**, 2205732.
21 J. Tang, A. D. Dysart and V. G. Pol, *Curr. Opin. Chem. Eng.*, 2015, **9**, 34–41.
22 S. Li, Z. Wang, J. Liu, L. Yang, Y. Guo, L. Cheng, M. Lei and W. Wang, *ACS Appl. Mater. Interfaces*, 2016, **8**, 19438–19445.
23 H. Xu, W. Wang, G. Yu, L. Qin, Y. Jiang, L. Ren and J. Chen, *ACS Appl. Energy Mater.*, 2020, **3**, 4738–4745.
24 Z. Zhang, Y. Huang, X. Liu, X. Wang and P. Liu, *Electrochim. Acta*, 2020, **342**, 136104.
25 H. Kim, D. Kim, Y. Lee, D. Byun, H.-S. Kim and W. Choi, *Chem. Eng. J.*, 2020, **383**, 123094.
26 S. H. Oh and J. S. Cho, *J. Alloys Compd.*, 2019, **806**, 1029–1038.
27 M. Han, J. Liu, C. Deng, J. Guo, Y. Mu, Z. Zou, K. Zheng, F. Yu, Q. Li and L. Wei, *Adv. Energy Mater.*, 2024, 2400246.
28 Y. Liu, Y. Qing, B. Zhou, L. Wang, B. Pu, X. Zhou, Y. Wang, M. Zhang, J. Bai and Q. Tang, *ACS Nano*, 2023, **17**, 2431–2439.
29 Z. Liu, T. Lu, T. Song, X.-Y. Yu, X. W. D. Lou and U. Paik, *Energy Environ. Sci.*, 2017, **10**, 1576–1580.
30 Y.-X. Wang, J. Yang, S.-L. Chou, H. K. Liu, W.-X. Zhang, D. Zhao and S. X. Dou, *Nat. Commun.*, 2015, **6**, 8689.
31 Y. B. Kim, H. Y. Seo, S. H. Kim, T. H. Kim, J. H. Choi, J. S. Cho, Y. C. Kang and G. D. Park, *Small Methods*, 2023, **7**, 2201370.
32 F. Xu, S. Li, S. Jing, X. Peng, L. Yuan, S. Lu, Y. Zhang and H. Fan, *J. Colloid Interface Sci.*, 2024, **660**, 907–915.
33 M. Song, D. Ye, W. Li, C. Lu, W. Wu and X. Wu, *ACS Appl. Mater. Interfaces*, 2024, **16**, 16120–16131.
34 J. Fu, S. Wang, D. Wu, J. Luo, C. Wang, J. Liang, X. Lin, Y. Hu, S. Zhang and F. Zhao, *Adv. Mater.*, 2024, **36**, 2308012.

35 J. Wang, H. Jing, X. Wang, Y. Xue, Q. Liang, W. Qi, H. Yu and C. F. Du, *Adv. Funct. Mater.*, 2024, 2315318.
36 J. Li, W. Zhang and W. Zheng, *Small*, 2024, **20**, 2305021.
37 X. Bai, T. Li, U. Gulzar, E. Venezia, L. Chen, S. Monaco, Z. Dang, M. Prato, S. Marras, P. Salimi, S. Fugattini, C. Capiglia and R. P. Zaccaria, *Nanoscale*, 2020, **12**, 15896–15904.
38 Y. Zhang, C. Wang, H. Hou, G. Zou and X. Ji, *Adv. Energy Mater.*, 2017, **7**, 1600173.
39 X. Song, X. Li, Z. Chen and Z. Wang, *Mater. Lett.*, 2020, **275**, 128109.
40 H. Liu, B. Liu, H. Guo, M. Liang, Y. Zhang, T. Borjigin, X. Yang, L. Wang and X. Sun, *Nano Energy*, 2018, **51**, 639–648.
41 L. Zhao, H.-H. Wu, C. Yang, Q. Zhang, G. Zhong, Z. Zheng, H. Chen, J. Wang, K. He and B. Wang, *ACS Nano*, 2018, **12**, 12597–12611.
42 R. Li, J. Huang, J. Li, L. Cao, Y. Luo, Y. He, G. Lu, A. Yu and S. Chen, *ChemElectroChem*, 2020, **7**, 604–613.
43 (*a*) H. Li, Y. He, Q. Wang, S. Gu, L. Wang, J. Yu, G. Zhou and L. Xu, *Adv. Energy Mater.*, 2023, **13**, 2302901; (*b*) A. B. Peng, Y. Li, J. Gao, F. Zhang, J. Li and G. Zhang, *J. Power Sources*, 2019, **437**, 226913.
44 Y. Zhang, J. Wang, L. Wang, L. Duan, G. Zhang, F. Zhao, X. Zhang and W. Lü, *J. Mater. Sci.*, 2020, **55**, 13102–13113.
45 J. Ru, T. He, B. Chen, Y. Feng, L. Zu, Z. Wang, Q. Zhang, T. Hao, R. Meng and R. Che, *Angew. Chem., Int. Ed.*, 2020, **59**, 14621–14627.
46 X.-K. Wang, J. Shi, L.-W. Mi, Y.-P. Zhai, J.-Y. Zhang, X.-M. Feng, Z.-J. Wu and W.-H. Chen, *Rare Met.*, 2020, **39**, 1053–1062.
47 Z. Liu, C. Wang, W. Yuan and Y. Xu, *Chin. J. Chem.*, 2024, **42**, 301–316.
48 S. Dong, Q. Su, W. Jiao, S. Ding, M. Zhang, G. Du and B. Xu, *J. Alloys Compd.*, 2020, 155888.
49 W. Mao, S. Zhang, F. Cao, J. Pan, Y. Ding, C. Ma, M. Li, Z. Hou, K. Bao and Y. Qian, *J. Alloys Compd.*, 2020, **842**, 155300.
50 H. Yang, L.-W. Chen, F. He, J. Zhang, Y. Feng, L. Zhao, B. Wang, L. He, Q. Zhang and Y. Yu, *Nano Lett.*, 2019, **20**, 758–767.
51 W. Liu, L. Du, S. Ju, X. Cheng, Q. Wu, Z. Hu and X. Yu, *ACS Nano*, 2021, **15**, 5679–5688.
52 K. Yang, H. Guo, M. Chen, B. Dong, C. Yan, J. Zai and X. Qian, *ACS Mater. Lett.*, 2023, **5**, 2683–2690.
53 J. Li, J. Cao, X. Li, H. M. K. Sari, L. Li, C. Lv, I. V. Zatovsky and W. Han, *Electrochim. Acta*, 2020, **332**, 135446.
54 G. Zhang, L. Yu, H. B. Wu, H. E. Hoster and X. W. Lou, *Adv. Mater.*, 2012, **24**, 4609–4613.
55 S. Santangelo, *Appl. Sci.*, 2019, **9**, 1049.
56 X. Guo, Y. Xue, H. Zhou, Y. Weng and J. Zhou, *ACS Appl. Mater. Interfaces*, 2019, **12**, 2407–2416.
57 Q. Huang, P. He, L. Xiao, Y. Feng, J. Liu, Y. Yang, B. Huang, X. Cui, P. Wang and W. Wei, *ACS Appl. Mater. Interfaces*, 2019, **12**, 2191–2198.
58 T. Famprikis, O. U. Kudu, J. Dawson, P. Canepa, F. Fauth, E. Suard, M. Zbiri, D. Dambournet, O. Borkiewicz and H. Bouyanfif, *J. Am. Chem. Soc.*, 2020, **142**, 18422–18436.
59 Z.-Y. Gu, J.-M. Cao, J.-Z. Guo, X.-T. Wang, X.-X. Zhao, S.-H. Zheng, Z.-H. Sun, J.-L. Yang, K.-Y. Zhang, H.-J. Liang, K. Li and X.-L. Wu, *J. Am. Chem. Soc.*, 2024, **146**, 4652–4664.
60 G. Åvall and P. Johansson, *J. Chem. Phys.*, 2020, **152**, 234104.
61 J. K. Kim and S.-K. Park, *J. Alloys Compd.*, 2024, 174373.
62 X. Geng, X. Hou, X. He and H. J. Fan, *Adv. Energy Mater.*, 2024, **14**, 2304094.
63 J. Li, L. Shi, J. Gao and G. Zhang, *Chem. – Eur. J.*, 2018, **24**, 1253–1258.
64 P. Ge, S. Li, L. Xu, K. Zou, X. Gao, X. Cao, G. Zou, H. Hou and X. Ji, *Adv. Energy Mater.*, 2019, **9**, 1803035.
65 Y. Zhong, X. Xia, F. Shi, J. Zhan, J. Tu and H. J. Fan, *Adv. Sci.*, 2016, **3**, 1500286.
66 P. Santhoshkumar, N. Shaji, M. Nanthagopal, J. W. Park, C. Senthil and C. W. Lee, *J. Power Sources*, 2020, **470**, 228459.
67 H. Jin, H. Wang, Z. Qi, D. S. Bin, T. Zhang, Y. Wan, J. Chen, C. Chuang, Y. R. Lu, T. S. Chan, H. Ju, A.-M. Cao, W. Yan, X. Wu, H. Ji and L.-J. Wan, *Angew. Chem., Int. Ed.*, 2020, **59**, 2318–2322.
68 Y. Zhang, Z. Wang, D. Li, Q. Sun, K. Lai, K. Li, Q. Yuan, X. Liu and L. Ci, *J. Mater. Chem. A*, 2020, **8**, 22874–22885.
69 J. Zhang, Y. Liu, H. Liu, Y. Song, S. Sun, Q. Li, X. Xing and J. Chen, *Small*, 2020, **16**, 2000504.
70 J. Ye, H. Zhao, M. Kang, W. Song, Q. Kong, C. Chen, R. Wu, J. Mi and Z. Li, *Chem. Commun.*, 2020, **56**, 1089–1092.
71 C. Wei, F. Luo, C. Zhang, H. Gao, J. Niu, W. Ma, Y. Bai and Z. Zhang, *Ionics*, 2019, 1–9.
72 W. Zhang, Z. Tu, J. Qian, S. Choudhury, L. A. Archer and Y. Lu, *Small*, 2018, **14**, 1703001.
73 G. Du, M. Tao, J. Li, T. Yang, W. Gao, J. Deng, Y. Qi, S. J. Bao and M. Xu, *Adv. Energy Mater.*, 2020, **10**, 1903351.
74 C. Luo, T. Shen, H. Ji, D. Huang, J. Liu, B. Ke, Y. Wu, Y. Chen and C. Yan, *Small*, 2020, **16**, 1906208.
75 L. Dashairya, D. Das, S. Jena, A. Mitra and P. Saha, *Nano Select*, 2021, **2**, 373–388.
76 A. Li, W. Zhu, C. Li, T. Wang and J. Gong, *Chem. Soc. Rev.*, 2019, **48**, 1874–1907.
77 Y.-A. Chen, Y.-T. Wang, H. S. Moon, K. Yong and Y.-J. Hsu, *RSC Adv.*, 2021, **11**, 12288–12305.
78 S. Liu, J. Feng, X. Bian, J. Liu, H. Xu and Y. An, *Energy Environ. Sci.*, 2017, **10**, 1222–1233.
79 R. Güttel, M. Paul and F. Schüth, *Catal. Sci. Technol.*, 2011, **1**, 65–68.
80 Y. Liu, J. Goebl and Y. Yin, *Chem. Soc. Rev.*, 2013, **42**, 2610–2653.
81 L. Yi, H. Wu, Y. Xu, J. Yu, Y. Zhao, H. Yang and C. Huang, *Nanoscale*, 2023, **15**, 127–143.
82 T. Harada, S. Ikeda, F. Hashimoto, T. Sakata, K. Ikeue, T. Torimoto and M. Matsumura, *Langmuir*, 2010, **26**, 17720–17725.
83 C. Chen, X. Fang, B. Wu, L. Huang and N. Zheng, *ChemCatChem*, 2012, **4**, 1578–1586.
84 Y.-L. Min, Y. Wan and S.-H. Yu, *Solid State Sci.*, 2009, **11**, 96–101.

85 M. Kim, J. C. Park, A. Kim, K. H. Park and H. Song, *Langmuir*, 2012, **28**, 6441–6447.
86 Y. Chen, H. Chen, D. Zeng, Y. Tian, F. Chen, J. Feng and J. Shi, *ACS Nano*, 2010, **4**, 6001–6013.
87 Y. N. Ko, Y. C. Kang and S. B. Park, *Chem. Commun.*, 2013, **49**, 3884–3886.
88 J. C. Park, J. Y. Kim, E. Heo, K. H. Park and H. Song, *Langmuir*, 2010, **26**, 16469–16473.
89 C.-H. Kuo, Y. Tang, L.-Y. Chou, B. T. Sneed, C. N. Brodsky, Z. Zhao and C.-K. Tsung, *J. Am. Chem. Soc.*, 2012, **134**, 14345–14348.
90 D. Cheng, X. Zhou, H. Xia and H. S. O. Chan, *Chem. Mater.*, 2005, **17**, 3578–3581.
91 N. Zhang, X. Fu and Y.-J. Xu, *J. Mater. Chem.*, 2011, **21**, 8152–8158.
92 Z. Teng, S. Wang, X. Su, G. Chen, Y. Liu, Z. Luo, W. Luo, Y. Tang, H. Ju and D. Zhao, *Adv. Mater. Interfaces*, 2014, **26**, 3741–3747.
93 Z. Teng, X. Su, Y. Zheng, J. Zhang, Y. Liu, S. Wang, J. Wu, G. Chen, J. Wang and D. Zhao, *J. Am. Chem. Soc.*, 2015, **137**, 7935–7944.
94 W. Zhou, Y. Yu, H. Chen, F. J. DiSalvo and H. C. D. Abruña, *J. Am. Chem. Soc.*, 2013, **135**, 16736–16743.
95 J. Lee, J. C. Park and H. Song, *Adv. Mater. Interfaces*, 2008, **20**, 1523–1528.
96 Y.-X. Wang, J. Yang, S.-L. Chou, H. K. Liu, W.-X. Zhang, D. Zhao and S. X. Dou, *Nat. Commun.*, 2015, **6**, 1–9.
97 H. Zhang, L. Zhou, O. Noonan, D. J. Martin, A. K. Whittaker and C. Yu, *Adv. Funct. Mater.*, 2014, **24**, 4337–4342.
98 S.-H. Wu, C.-T. Tseng, Y.-S. Lin, C.-H. Lin, Y. Hung and C.-Y. Mou, *J. Mater. Chem. A*, 2011, **21**, 789–794.
99 C.-H. Lin, X. Liu, S.-H. Wu, K.-H. Liu and C.-Y. Mou, *J. Phys. Chem. Lett.*, 2011, **2**, 2984–2988.
100 W. Dong, Y. Zhu, H. Huang, L. Jiang, H. Zhu, C. Li, B. Chen, Z. Shi and G. Wang, *J. Mater. Chem. A*, 2013, **1**, 10030–10036.
101 Z. Chen, J. Wang, G. Zhai, W. An and Y. Men, *Appl. Catal., B*, 2017, **218**, 825–832.
102 J. Liu, S. Z. Qiao, S. Budi Hartono and G. Q. Lu, *Angew. Chem., Int. Ed.*, 2010, **49**, 4981–4985.
103 Y. Ren, H. Shui, C. Peng, H. Liu and Y. Hu, *Fluid Phase Equilib.*, 2011, **312**, 31–36.
104 G. A. Carlson, J. P. McReynolds and F. H. Verhoek, *J. Am. Chem. Soc.*, 1945, **67**, 1334–1339.
105 H. Wu, S. Zhang, J. Zhang, G. Liu, J. Shi, L. Zhang, X. Cui, M. Ruan, Q. He and W. Bu, *Adv. Funct. Mater.*, 2011, **21**, 1850–1862.
106 J. Li, X. Liu, Z. Sun and L. Pan, *Ceram. Int.*, 2015, **41**, 8592–8598.
107 Y. Li, J. Lu, X. Cheng, H. Shi and Y. Zhang, *Nano Energy*, 2018, **48**, 441–447.
108 R. Purbia and S. Paria, *Nanoscale*, 2015, **7**, 19789–19873.
109 Y. Zhu, T. Ikoma, N. Hanagata and S. Kaskel, *Small*, 2010, **6**, 471–478.
110 Q. Sun, C. Z. Guo, G. H. Wang, W. C. Li, H. J. Bongard and A. H. Lu, *Chem. – Eur. J.*, 2013, **19**, 6217–6220.
111 X. W. Lou, D. Deng, J. Y. Lee and L. A. Archer, *Chem. Mater.*, 2008, **20**, 6562–6566.
112 Y.-L. Min, Y. Wan, R. Liu and S.-H. Yu, *Mater. Chem. Phys.*, 2008, **111**, 364–367.
113 Z.-M. Cui, Z. Chen, C.-Y. Cao, L. Jiang and W.-G. Song, *Chem. Commun.*, 2013, **49**, 2332–2334.
114 J. Liu, L. Yu, C. Wu, Y. Wen, K. Yin, F.-K. Chiang, R. Hu, J. Liu, L. Sun and L. Gu, *Nano Lett.*, 2017, **17**, 2034–2042.
115 Z. Li, Y. Fang, J. Zhang and X. W. Lou, *Adv. Mater. Interfaces*, 2018, **30**, 1800525.
116 Y. Zhu, Y. Fang and S. Kaskel, *J. Phys. Chem. C*, 2010, **114**, 16382–16388.
117 W. Ni, Y. Wang and R. Xu, *Part. Part. Syst. Charact.*, 2013, **30**, 873–880.
118 Z. Teng, X. Su, Y. Zheng, J. Sun, G. Chen, C. Tian, J. Wang, H. Li, Y. Zhao and G. Lu, *Chem. Mater.*, 2013, **25**, 98–105.
119 Y. Zeng, X. Wang, H. Wang, Y. Dong, Y. Ma and J. Yao, *Chem. Commun.*, 2010, **46**, 4312–4314.
120 W. Zhao and X. Ma, *ACS Sustainable Chem. Eng.*, 2020, **8**, 19040–19050.
121 A. Okada, D. Nagao, T. Ueno, H. Ishii and M. Konno, *Langmuir*, 2013, **29**, 9004–9009.
122 K. Zhang, X. Zhang, H. Chen, X. Chen, L. Zheng, J. Zhang and B. Yang, *Langmuir*, 2004, **20**, 11312–11314.
123 G. Li, E. Kang, K. Neoh and X. Yang, *Langmuir*, 2009, **25**, 4361–4364.
124 G. Liu, H. Wang, X. Yang and L. Li, *Eur. Polym. J.*, 2009, **45**, 2023–2032.
125 H.-f Ji, X.-x Wang, X. Zhang and X.-l Yang, *Chin. J. Polym. Sci.*, 2010, **28**, 807–817.
126 H. Li, L. Yang, J. Liu, S. Li, L. Fang, Y. Lu, H. Yang, S. Liu and M. Lei, *J. Power Sources*, 2016, **324**, 780–787.
127 Y. Zhao, J. Zhu, S. J. H. Ong, Q. Yao, X. Shi, K. Hou, Z. J. Xu and L. Guan, *Adv. Energy Mater.*, 2018, **8**, 1802565.
128 L. Ma, P. Yan, S. Wu, G. Zhu and Y. Shen, *J. Mater. Chem. A*, 2017, **5**, 16994–17000.
129 Y. Zhang, G. Hu, Q. Yu, Z. Liu, C. Yu, L. Wu, L. Zhou and L. Mai, *Mater. Chem. Front.*, 2020, **4**, 1656–1663.
130 Y. Zhang, C. Wang, H. Hou, G. Zou and X. Ji, *Adv. Energy Mater.*, 2017, **7**, 1600173.
131 Y. Zhang, A. Pan, L. Ding, Z. Zhou, Y. Wang, S. Niu, S. Liang and G. Cao, *ACS Appl. Mater. Interfaces*, 2017, **9**, 3624–3633.
132 Z. Li, Y. Fang, J. Zhang and X. W. Lou, *Adv. Mater.*, 2018, **30**, 1800525.
133 X. Xu, F. Li, D. Zhang, Z. Liu, S. Zuo, Z. Zeng and J. Liu, *Adv. Sci.*, 2022, **9**, 2200247.
134 J. Yang, T. Shao, C. Luo, J. Li, S. He, B. Meng, Q. Zhang, D. Zhang, Z. Xue and X. Zhou, *J. Alloys Compd.*, 2020, **834**, 155056.
135 X. Xia, Y. Wang, A. Ruditskiy and Y. Xia, *Adv. Mater.*, 2013, **25**, 6313–6333.
136 J. Park, T. Kwon, J. Kim, H. Jin, H. Y. Kim, B. Kim, S. H. Joo and K. Lee, *Chem. Soc. Rev.*, 2018, **47**, 8173–8202.
137 H. Cheng, C. Wang, D. Qin and Y. Xia, *Acc. Chem. Res.*, 2023, **56**, 900–909.

138 X. Kong, H. Wu, K. Lu, X. Zhang, Y. Zhu and H. Lei, *ACS Appl. Mater. Interfaces*, 2023, **15**, 41205–41223.
139 S. Xie, M. Jin, J. Tao, Y. Wang, Z. Xie, Y. Zhu and Y. Xia, *Chem. – Eur. J.*, 2012, **18**, 14974–14980.
140 Q. Shi, P. Zhang, Y. Li, H. Xia, D. Wang and X. Tao, *Chem. Sci.*, 2015, **6**, 4350–4357.
141 Y. Yin, R. M. Rioux, C. K. Erdonmez, S. Hughes, G. A. Somorjai and A. P. Alivisatos, *Science*, 2004, **304**, 711–714.
142 J. S. Cho and Y. C. Kang, *Small*, 2015, **11**, 4673–4681.
143 J. Gao, G. Liang, J. S. Cheung, Y. Pan, Y. Kuang, F. Zhao, B. Zhang, X. Zhang, E. X. Wu and B. Xu, *J. Am. Chem. Soc.*, 2008, **130**, 11828–11833.
144 E. V. Shevchenko, M. I. Bodnarchuk, M. V. Kovalenko, D. V. Talapin, R. K. Smith, S. Aloni, W. Heiss and A. P. Alivisatos, *Adv. Mater. Interfaces*, 2008, **20**, 4323–4329.
145 M. H. Oh, T. Yu, S.-H. Yu, B. Lim, K.-T. Ko, M.-G. Willinger, D.-H. Seo, B. H. Kim, M. G. Cho and J.-H. Park, *Science*, 2013, **340**, 964–968.
146 Y. Liu, B. Zhou, S. Liu, Q. Ma and W.-H. Zhang, *ACS Nano*, 2019, **13**, 5885–5892.
147 M. Kong, Y. Liu, B. Zhou, K. Yang, J. Tang, P. Zhang and W. H. Zhang, *Small*, 2020, **16**, 2001976.
148 L. Zhou, Y. Cheng, Q. Sun, L. Sun, C. Wang, X. Wang, D. Yin, L. Wang and J. Ming, *Chem. Commun.*, 2018, **54**, 4049–4052.
149 L. Yu, L. Zhang, J. Fu, J. Yun and K. H. Kim, *Chem. Eng. J.*, 2021, **417**, 129106.
150 G. Madras and B. J. McCoy, *J. Chem. Phys.*, 2003, **119**, 1683–1693.
151 A. Pan, H. B. Wu, L. Yu and X. W. Lou, *Angew. Chem., Int. Ed.*, 2013, **52**, 2226–2230.
152 B. Liu and H. C. Zeng, *Small*, 2005, **1**, 566–571.
153 W. Weng, J. Lin, Y. Du, X. Ge, X. Zhou and J. Bao, *J. Mater. Chem. A*, 2018, **6**, 10168–10175.
154 J. S. Chen, C. M. Li, W. W. Zhou, Q. Y. Yan, L. A. Archer and X. W. Lou, *Nanoscale*, 2009, **1**, 280–285.
155 Y. Ye, L. Kuai and B. Geng, *J. Mater. Chem. A*, 2012, **22**, 19132–19138.
156 L. Zhang, D. A. Blom and H. Wang, *Chem. Mater.*, 2011, **23**, 4587–4598.
157 W. Weng, J. Lin, Y. Du, X. Ge, X. Zhou and J. Bao, *J. Mater. Chem. A*, 2018, **6**, 10168–10175.
158 L. Zhao, X. Rong, Y. Niu, R. Xu, T. Zhang, T. Li, Y. Yu and Y. Hou, *Small*, 2020, **16**, 2004925.
159 G. D. Park and Y. C. Kang, *Small Methods*, 2021, **5**, 2100302.
160 S.-K. Park, J. K. Kim and Y. C. Kang, *J. Mater. Chem. A*, 2017, **5**, 18823–18830.
161 S. E. Skrabalak and K. S. Suslick, *J. Am. Chem. Soc.*, 2005, **127**, 9990–9991.
162 S. E. Skrabalak and K. S. Suslick, *J. Am. Chem. Soc.*, 2006, **128**, 12642–12643.
163 Z. Chen, L. Xu, Q. Chen, P. Hu, Z. Liu, Q. Yu, T. Zhu, H. Liu, G. Hu and Z. Zhu, *J. Mater. Chem. A*, 2019, **7**, 6740–6746.
164 J. Leng, Z. Wang, J. Wang, H.-H. Wu, G. Yan, X. Li, H. Guo, Y. Liu, Q. Zhang and Z. Guo, *Chem. Soc. Rev.*, 2019, **48**, 3015–3072.
165 S. H. Oh and J. S. Cho, *J. Alloys Compd.*, 2019, **806**, 1029–1038.
166 J. H. Kim and Y. C. Kang, *Nano Res.*, 2017, **10**, 3178–3188.
167 D. Guan, Q. Yu, C. Xu, C. Tang, L. Zhou, D. Zhao and L. Mai, *Nano Res.*, 2017, **10**, 4351–4359.
168 J. H. Choi, S. K. Park and Y. C. Kang, *Small*, 2019, **15**, 1803043.
169 Z. A. Qiao, Q. Huo, M. Chi, G. M. Veith, A. J. Binder and S. Dai, *Adv. Mater. Interfaces*, 2012, **24**, 6017–6021.
170 Y. Wang, L. Ling, W. Zhang, J. Guo, K. Ding, W. Duan and B. Liu, *Chem. Mater.*, 2019, **31**, 9546–9553.
171 A. Najafian, M. Rabbani, R. Rahimi, M. Deilamkamar and A. Maleki, *Solid State Sci.*, 2015, **46**, 7–13.
172 L. Guo, X. Cui, Y. Li, Q. He, L. Zhang, W. Bu and J. Shi, *Chem. – Asian J.*, 2009, **4**, 1480–1485.
173 X. W. Lou, C. Yuan, Q. Zhang and L. A. Archer, *Angew. Chem., Int. Ed.*, 2006, **45**, 3825–3829.
174 S. Ding, J. S. Chen, G. Qi, X. Duan, Z. Wang, E. P. Giannelis, L. A. Archer and X. W. Lou, *J. Am. Chem. Soc.*, 2011, **133**, 21–23.
175 R. V. Maligal-Ganesh, C. Xiao, T. W. Goh, L.-L. Wang, J. Gustafson, Y. Pei, Z. Qi, D. D. Johnson, S. Zhang and F. Tao, *ACS Catal.*, 2016, **6**, 1754–1763.
176 S. Luo, J. Ruan, Y. Wang, J. Hu, Y. Song, M. Chen and L. Wu, *Small*, 2021, **17**, 2101879.
177 J. Zhao, Y. Yang, C. Jiang, N. A. Khan, X. Jia, H. Zhao and S. Ding, *Nanotechnology*, 2021, **32**, 505602.
178 K. Kaviyarasu, M. M. Maaza, E. Manikandan and J. Kennedy, *Adv. Mater. Lett.*, 2016, **7**, 684–696.
179 A. Khanal, Y. Inoue, M. Yada and K. Nakashima, *J. Am. Chem. Soc.*, 2007, **129**, 1534–1535.
180 H. Chen, C. Deng and X. Zhang, *Angew. Chem., Int. Ed.*, 2010, **49**, 607–611.
181 M. H. R. Farimani, N. Shahtahmasebi, M. R. Roknabadi, N. Ghows and A. Kazemi, *Phys. E*, 2013, **53**, 207–216.
182 G. S. Chaubey and J.-K. Kim, *Bull. Korean Chem. Soc.*, 2007, **28**, 2279–2282.
183 X. Ren, Y. Yao, P. Ren, Y. Wang and Y. Peng, *Mater. Lett.*, 2019, **238**, 286–289.
184 P.-W. Xiao, L. Zhao, Z.-Y. Sui and B.-H. Han, *Langmuir*, 2017, **33**, 6038–6045.
185 W. Duan, Z. Zhu, H. Li, Z. Hu, K. Zhang, F. Cheng and J. Chen, *J. Mater. Chem. A*, 2014, **2**, 8668–8675.
186 S. Tao, P. Cui, W. Huang, Z. Yu, X. Wang, S. Wei, D. Liu, L. Song and W. Chu, *Carbon*, 2016, **96**, 1028–1033.
187 H. Kang, Y. Liu, M. Shang, T. Lu, Y. Wang and L. Jiao, *Nanoscale*, 2015, **7**, 9261–9267.
188 H. Liu, W. Pei, W.-H. Lai, Z. Yan, H. Yang, Y. Lei, Y.-X. Wang, Q. Gu, S. Zhou and S. Chou, *ACS Nano*, 2020, **14**, 7259–7268.
189 M. Mostafa, Z. Alrowaili, G. Rashwan and M. Gerges, *Heliyon*, 2020, **6**, e03389.
190 J. Flores, V. Torres, M. Popa, D. Crespo and J. Calderón-Moreno, *J. Non-Cryst. Solids*, 2008, **354**, 5435–5439.
191 A. Bai, H. Song, G. He, Q. Li, C. Yang, L. Tang and Y. Yu, *Ceram. Int.*, 2016, **42**, 7583–7592.

192 X. Guo, Y. Deng, D. Gu, R. Che and D. Zhao, *J. Mater. Chem.*, 2009, **19**, 6706–6712.
193 J. Yang, Y. Deng, Q. Wu, J. Zhou, H. Bao, Q. Li, F. Zhang, F. Li, B. Tu and D. Zhao, *Langmuir*, 2010, **26**, 8850–8856.
194 J. Yang, F. Zhang, Y. Chen, S. Qian, P. Hu, W. Li, Y. Deng, Y. Fang, L. Han and M. Luqman, *Chem. Commun.*, 2011, **47**, 11618–11620.
195 W. Zhao, M. Lang, Y. Li, L. Li and J. Shi, *J. Mater. Chem. A*, 2009, **19**, 2778–2783.
196 F. Xie, L. Zhang, D. Su, M. Jaroniec and S. Z. Qiao, *Adv. Mater.*, 2017, **29**, 1700989.
197 X. Chen, Y. Fang, H. Lu, H. Li, X. Feng, W. Chen, X. Ai, H. Yang and Y. Cao, *Small*, 2021, **17**, 2102248.
198 W. Meng, Z. Dang, D. Li, L. Jiang and D. Fang, *Adv. Energy Mater.*, 2022, **12**, 2201531.
199 J. Zhang, T. He, W. Zhang, J. Sheng, I. S. Amiinu, Z. Kou, J. Yang, L. Mai and S. Mu, *Adv. Energy Mater.*, 2017, **7**, 1602092.
200 Y. Zhao, F. Wang, C. Wang, S. Wang, C. Wang, Z. Zhao, L. Duan, Y. Liu, Y. Wu and W. Li, *Nano Energy*, 2019, **56**, 426–433.
201 Z. Cui, S. A. He, J. Zhu, M. Gao, H. Wang, H. Zhang and R. Zou, *Small Methods*, 2022, **6**, 2101484.
202 H. Xu, L. Qin, J. Chen, Z. Wang, W. Zhang, P. Zhang, W. Tian, Y. Zhang, X. Guo and Z. Sun, *J. Mater. Chem. A*, 2018, **6**, 13153–13163.
203 Y. Zhang, A. Pan, L. Ding, Z. Zhou, Y. Wang, S. Niu, S. Liang and G. Cao, *ACS Appl. Mater. Interfaces*, 2017, **9**, 3624–3633.
204 L. Wang, Z. Han, Q. Zhao, X. Yao, Y. Zhu, X. Ma, S. Wu and C. Cao, *J. Mater. Chem. A*, 2020, **8**, 8612–8619.
205 Q. Chen, S. Sun, T. Zhai, M. Yang, X. Zhao and H. Xia, *Adv. Energy Mater.*, 2018, **8**, 1800054.
206 T. Wang, P. Hu, C. Zhang, H. Du, Z. Zhang, X. Wang, S. Chen, J. Xiong and G. Cui, *ACS Appl. Mater. Interfaces*, 2016, **8**, 7811–7817.
207 D. Zhang, W. Sun, Y. Zhang, Y. Dou, Y. Jiang and S. X. Dou, *Adv. Funct. Mater.*, 2016, **26**, 7479–7485.
208 Z. Sun, X. Wu, Z. Gu, P. Han, B. Zhao, D. Qu, L. Gao, Z. Liu, D. Han and L. Niu, *Carbon*, 2020, **166**, 175–182.
209 X. Wang, J. Zhao, Y. Chen, X. Zhang, K. Zhu, Q. Wang, J. Yan, D. Cao and G. Wang, *Small*, 2024, **20**, 2307747.
210 Y. Zhang, C. Wang, H. Hou, G. Zou and X. Ji, *Adv. Energy Mater.*, 2017, **7**, 1600173.
211 X. Hu, X. Liu, K. Chen, G. Wang and H. Wang, *J. Mater. Chem. A*, 2019, **7**, 11016–11037.
212 G. Wang, Y. Zhang, B. Guo, L. Tang, G. Xu, Y. Zhang, M. Wu, H.-K. Liu, S.-X. Dou and C. Wu, *Nano Lett.*, 2020, **20**, 4464–4471.
213 N. Zhu, X. Mao, G. Wang, M. Zhu, H. Wang, G. Xu, M. Wu, H. K. Liu, S.-X. Dou and C. Wu, *J. Mater. Chem. A*, 2021, **9**, 13200–13208.
214 F. Ma, P. Hu, T. Wang, J. Liang, R. Han, J. Han and Q. Li, *ACS Appl. Energy Mater.*, 2021, **4**, 3487–3494.
215 M. K. Aslam, T. Hussain, H. Tabassum, Z. Wei, W. Tang, S. Li, S.-J. Bao, X. S. Zhao and M. Xu, *Chem. Eng. J.*, 2022, **429**, 132389.
216 G. Wang, Y. Zhang, B. Guo, L. Tang, G. Xu, Y. Zhang, M. Wu, H.-K. Liu, S.-X. Dou and C. Wu, *Nano Lett.*, 2020, **20**, 4464–4471.
217 W. Liu, X. Yuan and X. Yu, *Nanoscale*, 2018, **10**, 16675–16682.
218 S. Dong, C. Li, Z. Li, L. Zhang and L. Yin, *Small*, 2018, **14**, 1704517.
219 F. Bu, P. Xiao, J. Chen, M. F. A. Aboud, I. Shakir and Y. Xu, *J. Mater. Chem. A*, 2018, **6**, 6414–6421.
220 Y. Han, J. Li, T. Zhang, P. Qi, S. Li, X. Gao, J. Zhou, X. Feng and B. Wang, *Chem. – Eur. J.*, 2018, **24**, 1651–1656.
221 Y. Cai, H.-E. Wang, X. Zhao, F. Huang, C. Wang, Z. Deng, Y. Li, G. Cao and B.-L. Su, *ACS Appl. Mater. Interfaces*, 2017, **9**, 10652–10663.
222 W. Zhao, C. Guo and C. M. Li, *J. Mater. Chem. A*, 2017, **5**, 19195–19202.
223 L. Shi, D. Li, J. Yu, H. Liu, Y. Zhao, H. Xin, Y. Lin, C. Lin, C. Li and C. Zhu, *J. Mater. Chem. A*, 2018, **6**, 7967–7976.
224 J. Zhang, K. Zhang, J. Yang, G. H. Lee, J. Shin, V. Wing-hei Lau and Y. M. Kang, *Adv. Energy Mater.*, 2018, **8**, 1800283.
225 S. Wen, J. Zhao, J. Chen, J. Yang and J. Xu, *Dalton Trans.*, 2019, **48**, 10448–10454.
226 X. Wang, L. Fan, D. Gong, J. Zhu, Q. Zhang and B. Lu, *Adv. Funct. Mater.*, 2016, **26**, 1104–1111.
227 H. Y. Chen, N. Bucher, S. Hartung, L. Li, J. Friedl, H. P. Liou, C. L. Sun, U. Stimming and M. Srinivasan, *Adv. Mater. Interfaces*, 2016, **3**, 1600357.
228 S. Dong, C. Li, X. Ge, Z. Li, X. Miao and L. Yin, *ACS Nano*, 2017, **11**, 6474–6482.
229 H. Wan, J. P. Mwizerwa, X. Qi, X. Liu, X. Xu, H. Li, Y.-S. Hu and X. Yao, *ACS Nano*, 2018, **12**, 2809–2817.
230 G. D. Moon, *Nanomaterials*, 2020, **10**, 675.
231 G. K. Veerasubramani, Y. Subramanian, M.-S. Park, G. Nagaraju, B. Senthilkumar, Y.-S. Lee and D.-W. Kim, *J. Mater. Chem. A*, 2018, **6**, 20056–20068.
232 Y. N. Ko, S. Choi, S. Park and Y. C. Kang, *Nanoscale*, 2014, **6**, 10511–10515.
233 Q. Chen, S. Sun, T. Zhai, M. Yang, X. Zhao and H. Xia, *Adv. Energy Mater.*, 2018, **8**, 1800054.
234 F. Sun, Q. Ma, M. Kong, X. Zhou, Y. Liu, B. Zhou, P. Zhang and W.-H. Zhang, *RSC Adv.*, 2018, **8**, 36826–36830.
235 M. Wang, Y. Huang, Y. Zhu, N. Zhang, J. Zhang, X. Qin and H. Zhang, *Electrochim. Acta*, 2020, **335**, 135694.
236 W. Weng, J. Xu, C. Lai, Z. Xu, Y. Du, J. Lin and X. Zhou, *J. Alloys Compd.*, 2020, **817**, 152732.
237 M. Chen, Z. Zhang, L. Si, R. Wang and J. Cai, *ACS Appl. Mater. Interfaces*, 2019, **11**, 35050–35059.
238 Q. Li, L. Li, K. A. Owusu, W. Luo, Q. An, Q. Wei, Q. Zhang and L. Mai, *Nano Energy*, 2017, **41**, 109–116.
239 J. Zheng, X. Huang, X. Pan, C. Teng and N. Wang, *Appl. Surf. Sci.*, 2019, **473**, 699–705.
240 P. Jing, Q. Wang, B. Wang, X. Gao, Y. Zhang and H. Wu, *Carbon*, 2020, **159**, 366–377.
241 J. Wang, L. Zhu, F. Li, T. Yao, T. Liu, Y. Cheng, Z. Yin and H. Wang, *Small*, 2020, **16**, 2002487.

242 P. Nie, G. Xu, J. Jiang, H. Dou, Y. Wu, Y. Zhang, J. Wang, M. Shi, R. Fu and X. Zhang, *Small Methods*, 2018, **2**, 1700272.
243 A. B. D. Nandiyanto and K. Okuyama, *Adv. Powder Technol.*, 2011, **22**, 1–19.
244 T. Cheng, J. Xu, Z. Tan, J. Ye, Z. Tao, Z. Du, Y. Wu, S. Wu, H. Ji and Y. Yu, *Energy Storage Mater.*, 2018, **10**, 282–290.
245 D. S. Jung, S. B. Park and Y. C. Kang, *Korean J. Chem. Eng.*, 2010, **27**, 1621–1645.
246 M. H. Aghaali and S. Firoozi, *Int. J. Hydrogen Energy*, 2021, **46**, 357–373.
247 Y. Zhu, S. H. Choi, X. Fan, J. Shin, Z. Ma, M. R. Zachariah, J. W. Choi and C. Wang, *Adv. Energy Mater.*, 2017, **7**, 1601578.
248 Y. Liu, N. Zhang, L. Jiao, Z. Tao and J. Chen, *Adv. Funct. Mater.*, 2015, **25**, 214–220.
249 G. D. Park and Y. C. Kang, *Chem. – Eur. J.*, 2016, **22**, 4140–4146.
250 J. K. Kim, S. Y. Jeong, S. H. Lim, J. H. Oh, S. K. Park, J. S. Cho and Y. C. Kang, *Chem. – Asian J.*, 2019, **14**, 3127–3140.
251 C. Yang, W. Li, Z. Yang, L. Gu and Y. Yu, *Nano Energy*, 2015, **18**, 12–19.
252 J. Wang, J. Li, X. He, X. Zhang, B. Yan, X. Hou, L. Du, T. Placke, M. Winter and J. Li, *J. Power Sources*, 2020, **461**, 228129.
253 Q. Li, Q. Jiao, W. Zhou, X. Feng, Q. Shi, Z. Dai, T. Gu, Y. Zhao, H. Li and C. Feng, *Mater. Chem. Front.*, 2021, **5**, 293–303.
254 Z. Zhao, C. Li, Z. Liu and D. Li, *Int. J. Hydrogen Energy*, 2021, **46**, 26457–26465.
255 G. Chen, X. Li, T. Zeng, R. Han and Q. Wang, *Carbon*, 2021, **171**, 464–473.
256 B. Wang, Y. Cheng, H. Su, M. Cheng, Y. Li, H. Geng and Z. Dai, *ChemSusChem*, 2020, **13**, 4078–4085.
257 J. Liu, L. Yu, C. Wu, Y. Wen, K. Yin, F.-K. Chiang, R. Hu, J. Liu, L. Sun and L. Gu, *Nano Lett.*, 2017, **17**, 2034–2042.
258 Y.-X. Wang, J. Yang, S.-L. Chou, H. K. Liu, W.-X. Zhang, D. Zhao and S. X. Dou, *Nat. Commun.*, 2015, **6**(8689), 1–9.
259 W. Zhao, C. Guo and C. M. Li, *J. Mater. Chem. A*, 2017, **5**, 19195–19202.
260 H. Geng, J. Yang, Z. Dai, Y. Zhang, Y. Zheng, H. Yu, H. Wang, Z. Luo, Y. Guo and Y. Zhang, *Small*, 2017, **13**, 1603490.
261 J. Gao, Y. Li, Y. Liu, S. Jiao, J. Li, G. Wang, S. Zeng and G. Zhang, *J. Mater. Chem. A*, 2019, **7**, 18828–18834.
262 Y. Lin, X. Guo, M. Hu, B. Liu, Y. Dong, X. Wang, N. Li and H.-E. Wang, *Nanoscale*, 2020, **12**, 14689–14698.
263 S. H. Choi and Y. C. Kang, *ACS Appl. Mater. Interfaces*, 2015, **7**, 24694–24702.
264 X. Han, M. Ouyang, L. Lu, J. Li, Y. Zheng and Z. Li, *J. Power Sources*, 2014, **251**, 38–54.
265 Z. Wei, Q. He and Y. Zhao, *J. Power Sources*, 2022, **549**, 232125.
266 Z. H. Shen, H. X. Liu, Y. Shen, J. M. Hu, L. Q. Chen and C. W. Nan, *Interdiscip. Mater.*, 2022, **1**, 175–195.
267 D. Roman, S. Saxena, V. Robu, M. Pecht and D. Flynn, *Nat. Mach. Intell.*, 2021, **3**, 447–456.
268 M. Berecibar, *Nature*, 2019, **568**, 325–326.
269 Z. Fei, F. Yang, K.-L. Tsui, L. Li and Z. Zhang, *Energy*, 2021, **225**, 120205.
270 B. Oral, B. Tekin, D. Eroglu and R. Yildirim, *Assessment of Na-Ion Battery Performance Using Machine Learning, Electrochemical Society Meeting Abstracts 243*, The Electrochemical Society, Inc., 2023, pp. 882–882.
271 B. Oral, B. Tekin, D. Eroglu and R. Yildirim, *J. Power Sources*, 2022, **549**, 232126.
272 Y. Zhang, T. Zhan, Y. Sun, L. Lu and B. Chen, *ChemSusChem*, 2023, e202301284.
273 X. Liu, T. Wang, T. Ji, H. Wang, H. Liu, J. Li and D. Chao, *J. Mater. Chem. A*, 2022, **10**, 8031–8046.
274 B. Peng, Z. Sun, S. Jiao, G. Wang and G. Zhang, *Batteries Supercaps*, 2020, **3**, 147–154.
275 B. Peng, Z. Sun, L. Zhao, J. Li and G. Zhang, *Energy Storage Mater.*, 2021, **35**, 620–629.
276 S. Yang, S. Hu, J. Zhao, H. Cui, Y. Wang, S. Zhao, C. Lan and Z. Dong, *Energy Technol.*, 2022, **10**, 2200733.
277 H. Wu, J. Hao, Y. Jiang, Y. Jiao, J. Liu, X. Xu, K. Davey, C. Wang and S.-Z. Qiao, *Nat. Commun.*, 2024, **15**, 575.
278 K. Abraham, *ACS Energy Lett.*, 2020, **5**, 3544–3547.
279 S. Fan, S. Huang, Y. Chen, Y. Shang, Y. Wang, D. Kong, M. E. Pam, L. Shi, Y. W. Lim and Y. Shi, *Energy Storage Mater.*, 2019, **23**, 17–24.
280 Q. Chen, S. Sun, T. Zhai, M. Yang, X. Zhao and H. Xia, *Adv. Energy Mater.*, 2018, **8**, 1800054.
281 G. Zhao, Y. Zhang, L. Yang, Y. Jiang, Y. Zhang, W. Hong, Y. Tian, H. Zhao, J. Hu and L. Zhou, *Adv. Funct. Mater.*, 2018, **28**, 1803690.
282 Q. Zhou, Y. Wang, R. Ou, X. Ding, Y. Xin, F. Wu and H. Gao, *Small*, 2024, 2310699, DOI: **10.1002/smll.202310699**.
283 L. Wang, Z. Han, Q. Zhao, X. Yao, Y. Zhu, X. Ma, S. Wu and C. Cao, *J. Mater. Chem. A*, 2020, **8**, 8612–8619.
284 Z. Man, P. Li, D. Zhou, Y. Wang, X. Liang, R. Zang, P. Li, Y. Zuo, Y. M. Lam and G. Wang, *Nano Lett.*, 2020, **20**, 3769–3777.
285 X. Chen, D. Wang and J. Chen, *New J. Chem.*, 2019, **43**, 10291–10296.
286 B. Chen, H. Qin, K. Li, B. Zhang, E. Liu, N. Zhao, C. Shi and C. He, *Nano Energy*, 2019, **66**, 104133.
287 R. Zang, P. Li, X. Guo, Z. Man, S. Zhang, C. Wang and G. Wang, *J. Mater. Chem. A*, 2019, **7**, 14051–14059.
288 Z. Chen, L. Xu, Q. Chen, P. Hu, Z. Liu, Q. Yu, T. Zhu, H. Liu, G. Hu and Z. Zhu, *J. Mater. Chem. A*, 2019, **7**, 6740–6746.
289 J. Song, D. Xiao, H. Jia, G. Zhu, M. Engelhard, B. Xiao, S. Feng, D. Li, D. Reed and V. L. Sprenkle, *Nanoscale*, 2019, **11**, 348–355.
290 X. Li, Y. Zhao, Q. Yao and L. Guan, *Electrochim. Acta*, 2018, **270**, 1–8.
291 J. Song, P. Yan, L. Luo, X. Qi, X. Rong, J. Zheng, B. Xiao, S. Feng, C. Wang and Y.-S. Hu, *Nano Energy*, 2017, **40**, 504–511.

292 S. Qiu, L. Xiao, X. Ai, H. Yang and Y. Cao, *ACS Appl. Mater. Interfaces*, 2017, **9**, 345–353.
293 H. Yan, Y. Fu, X. Wu, X. Xue, C. Li and L. Zhang, *Solid State Ionics*, 2019, **336**, 95–101.
294 H. Tian, Y. Liang, J. Repac, S. Zhang, C. Luo, S.-C. Liou, G. Wang, S. H. Ehrman and W. Han, *J. Phys. Chem. C*, 2018, **122**, 22232–22240.
295 F. Xie, L. Zhang, Q. Gu, D. Chao, M. Jaroniec and S.-Z. Qiao, *Nano Energy*, 2019, **60**, 591–599.
296 S. Yao, J. Cui, Z. Lu, Z. L. Xu, L. Qin, J. Huang, Z. Sadighi, F. Ciucci and J. K. Kim, *Adv. Energy Mater.*, 2017, **7**, 1602149.
297 Y. Cao, D. Fang, X. Liu, Z. Luo, G. Li, W. Xu, M. Jiang and C. Xiong, *Compos. Sci. Technol.*, 2016, **137**, 130–137.
298 Z. Zhang, J. Zhang, X. Zhao and F. Yang, *Carbon*, 2015, **95**, 552–559.
299 X. Zhao, Z. Zhang, F. Yang, Y. Fu, Y. Lai and J. Li, *RSC Adv.*, 2015, **5**, 31465–31471.
300 X. Miao, R. Yin, X. Ge, Z. Li and L. Yin, *Small*, 2017, **13**, 1702138.
301 E. Lim, C. Jo, M. S. Kim, M. H. Kim, J. Chun, H. Kim, J. Park, K. C. Roh, K. Kang and S. Yoon, *Adv. Funct. Mater.*, 2016, **26**, 3711–3719.
302 Q. Pan, F. Zheng, Y. Liu, Y. Li, W. Zhong, G. Chen, J. Hu, C. Yang and M. Liu, *J. Mater. Chem. A*, 2019, **7**, 20229–20238.
303 Y. Zhang, H. Gao, J. Niu, W. Ma, Y. Shi, M. Song, Z. Peng and Z. Zhang, *ACS Nano*, 2018, **12**, 11678–11688.
304 X. Ma, X. Xiong, P. Zou, W. Liu, F. Wang, L. Liang, Y. Liu, C. Yuan and Z. Lin, *Small*, 2019, **15**, 1903259.
305 H. Y. Seo, J. H. Choi, Y. B. Kim, J. S. Cho, Y. C. Kang and G. D. Park, *J. Mater. Chem. A*, 2023, **11**, 24738–24753.
306 N. Wang, Z. Bai, Y. Qian and J. Yang, *ACS Appl. Mater. Interfaces*, 2017, **9**, 447–454.
307 J. Feng, S.-H. Luo, Y. Zhan, S.-X. Yan, P.-W. Li, L. Zhang, Q. Wang, Y.-H. Zhang and X. Liu, *ACS Appl. Mater. Interfaces*, 2021, **13**, 51095–51106.
308 X. Hu, X. Liu, K. Chen, G. Wang and H. Wang, *J. Mater. Chem. A*, 2019, **7**, 11016–11037.
309 H. Liang, X. Li, Z. Liu, W. Yang, X. Liu, Y. Zhang and H. Fan, *Mater. Chem. Front.*, 2022, **6**, 194–202.
310 J. Feng, S. h Luo, S. x Yan, Y. Zhan, Q. Wang, Y. h Zhang, X. Liu and L. j Chang, *Small*, 2021, **17**, 2101887.
311 Y. Zhao, X. Shi, S. J. H. Ong, Q. Yao, B. Chen, K. Hou, C. Liu, Z. J. Xu and L. Guan, *ACS Nano*, 2020, **14**, 4463–4474.
312 M. Chen, Z. Zhang, L. Si, R. Wang and J. Cai, *ACS Appl. Mater. Interfaces*, 2019, **11**, 35050–35059.
313 W. Zhao, X. Wang, X. Ma, L. Yue, Q. Liu, Y. Luo, Y. Liu, A. M. Asiri and X. Sun, *J. Mater. Chem. A*, 2021, **9**, 15807–15819.
314 N. Zhu, X. Mao, G. Wang, M. Zhu, H. Wang, G. Xu, M. Wu, H. K. Liu, S.-X. Dou and C. Wu, *J. Mater. Chem. A*, 2021, **9**, 13200–13208.